Research Square

Preprints are preliminary reports that have not undergone peer review.
They should not be considered conclusive, used to inform clinical practice,
or referenced by the media as validated information.

A decade of rainfall- and earthquake-triggered multiple-occurrence landslide events in the Colombian Andes (2015–2025): compilation and spatial analysis

Emanuel Castillo-Cardona

eecastilloc@unal.edu.co

EAFIT University: Universidad EAFIT https://orcid.org/0009-0003-2391-1237

Daniel F. Ruiz

EAFIT University: Universidad EAFIT

Exneyder A. Montoya-Araque

EAFIT University: Universidad EAFIT

Marco F. Gamboa

EAFIT University: Universidad EAFIT

Alejandro Marulanda-Tobon

EAFIT University: Universidad EAFIT

Research Article

Keywords: landslide inventory, Sentinel-2, spatial analysis, tropical mountains

Posted Date: November 13th, 2026

DOI: https://doi.org/10.21203/rs.3.rs-11167923/v1

License: This work is licensed under a Creative Commons Attribution 4.0 International License.
Read Full License

A decade of rainfall- and earthquake-triggered multiple-occurrence landslide events in the Colombian Andes (2015–2025): compilation and spatial analysis

Emanuel Castillo-Cardona[1*] Daniel F. Ruiz[2] Exneyder A. Montoya-Araque[1]
Marco F. Gamboa-Ramirez[1] Alejandro Marulanda-Tobon[2]

[1] Proyecto SAMA, Universidad EAFIT, Carrera 49 N° 7 Sur-50, Medellín, Colombia; ecastilloc@eafit.edu.co (E.C.); eamontoyaa@eafit.edu.co (E.M.); mgamboa@eafit.edu.co (M.G.)

[2] School of Applied Sciences and Engineering, Universidad EAFIT, Carrera 49 N° 7 Sur-50, Medellín, Colombia; dfruizr@eafit.edu.co (D.R.); amarula2@eafit.edu.co (A.M.)

Correspondence: ecastilloc@eafit.edu.co

Abstract

Multiple-occurrence regional landslide events, in which hundreds or thousands of landslides occur simultaneously and alter the landscape across considerable areas, have increased in frequency, or at least the number of reported events, in recent decades in the Colombian Andes. However, their spatial and geomorphological characteristics remain poorly documented for most events. In this study, we compiled 13 multiple-occurrence landslides that occurred between 2015 and 2025. The dataset was constructed by manually delineating pre- and post-event Sentinel-2 compositions, complemented by previous inventories, resulting in a total of 8,088 landslide samples. Each event was analyzed using morphometric, lithological, spatial density, precipitation, and multivariate approaches to identify common patterns. The results show that four morphometric variables consistently separate the thirteen inventories: slope, distance to drainage, roughness, and flow accumulation. Intrusive igneous rocks were the most frequent lithological setting, occurring in seven of the 13 events, while more than 70% of the mapped landslides occurred on coarse-grained soils. The spatial density patterns were different in the triggering factor types: events triggered by rain resulted in elongated clusters with dense cores; earthquake, scattered and disconnected cores with less density. Rainfall

*Corresponding author: ecastilloc@eafit.edu.co

analysis revealed that most rainfall-triggered events occurred under neutral ENSO conditions. This study provides a regional dataset and framework for exploring these landslide events in the Colombian Andes. The findings show that the events share a common geomorphological setting, but their spatial organization and magnitude vary substantially among events. The resulting inventories are openly available and provide a foundation for expanding comparative studies as new multiple-occurrence events are documented.

Keywords: landslide inventory; Sentinel-2; spatial analysis; tropical mountains

1 Introduction

A multiple-occurrence regional landslide event (MORLE) is a term referring to the simultaneous triggering of hundreds to thousands of landslides within a short window of time and across a specific area ranging from tens to thousands of square kilometers (Crozier, 2017). Massive scales of this phenomenon have been documented over the years. The 2008 Wenchuan earthquake triggered around 197,000 landslides over approximately 35,000 km^2 (Xu et al., 2014; Huang and Fan, 2013; Li et al., 2014); another example was Typhoon Morakot, which produced at least 22,705 landslides covering 274 km^2 in southern Taiwan in 2009 (Lin et al., 2011). The implications of these events range from changes in the rate of landscape erosion (Hovius et al., 2011; Dadson et al., 2004), severe impacts on ecosystems (Restrepo et al., 2009), to direct and irreparable damage to communities and civil infrastructure (Sepúlveda and Petley, 2015). Furthermore, it initiates a multi-hazard cascade process that can last for years (Fan et al., 2019), such as sediment transport (Hovius et al., 2011), channel dams (Costa and Schuster, 1988), and the subsequent evolution of landslides into debris flows (Zhang and Zhang, 2017).

This type of event has allowed for the compilation of inventories with thousands of samples for the study of the phenomenon, yielding information on the distribution of landslide sizes (Malamud et al., 2004; Tanyaş et al., 2018), spatial patterns in the concentration of the event (Crozier, 2017; Dai et al., 2011), and differences between triggering factors (Meunier et al., 2008; Marc et al., 2015). In the last decade, numerous efforts have focused on exploring these events in different parts of the world (Meena et al., 2023; Vershel and Kirschbaum, 2025; Arango-Carmona et al., 2025), although most of the information is concentrated where events of considerable magnitude have occurred (Tanyaş et al., 2017). In Asia, particularly in Japan, Taiwan, China, the Philippines, and Indonesia, a large proportion of the landslide events and research efforts are found, reflecting both the high frequency of rainfall- and earthquake-triggered landslides and

the availability of long-term inventories in these regions (Kirschbaum et al., 2010; Froude and Petley, 2018; Tehrani et al., 2022). This has also enabled considerable progress in subsequent applications, such as rainfall thresholds (Saito et al., 2010; Dahal and Hasegawa, 2008; Segoni et al., 2018) and automatic landslide detection (Ghorbanzadeh et al., 2022).

Much of the current understanding of the characteristics of MORLEs is concentrated in a limited number of mountainous terrains (Tanyaş et al., 2017; Froude and Petley, 2018), while other regions remain comparatively underreported (Kirschbaum et al., 2010; Sepúlveda and Petley, 2015). The Colombian Andes, due to their equatorial location, like other tropical mountain ranges, are highly prone to this phenomenon because they combine a series of intertropical hydrometeorological patterns (Poveda et al., 2006; Aristízabal and Sánchez, 2020) with geological and geomorphological configurations such as the interaction of multiple tectonic plates, dissected mountain terrain, and highly weathered soil profiles (Palacio Cordoba et al., 2020; Aristízabal and Korup, 2025). Some studies have focused primarily on the spatial and temporal understanding of individual events, such as the geospatial analysis of 838 landslides following an M_w 6.0 earthquake, where the landslide locations shared common characteristics in terms of their topographic position (García-Delgado and Contreras, 2021). Other studies focus on those triggered by rainfall. One of the first recorded was the La Arenosa event on 21 September 1990 (Hermelin et al., 1992), where hundreds of landslides evolved into a torrential flow that destroyed a power plant and affected hundreds of people. More recently, over a two-year period, Colombia experienced two of the most catastrophic cascading events of recent decades. The first, on 18 May 2015, was a debris flood in the La Liboriana River in Salgar, triggered by 112 landslides in the upper part of the basin (Gómez Cardona et al., 2025), following the unusual occurrence of two rainstorms within a single day (Velásquez et al., 2020).. The second occurred on 31 March 2017, when 1,082 landslides were triggered by four days of accumulated rainfall that culminated in a high-intensity storm (Prada-Sarmiento et al., 2019a). The landslides then evolved into a debris flow and flash flood, causing hundreds of deaths and affecting thousands.

The term *shallow landslides cluster* has been used in the Colombian Andes to describe events consisting of hundreds of failures occurring in the same basin or set of slopes with similar topographic characteristics (Palacio Cordoba, 2023), which subsequently evolve into debris flows and flash floods (Aristízabal and Sánchez, 2020; Arango-Carmona et al., 2025). Despite their recurrence, most of these events remain without an available inventory and, therefore, without consistent progress toward understanding their occurrence. This is largely due to the fact that

many of them occur in remote rural regions, where the reach and interest of institutions are limited (García-Delgado et al., 2022; Aristízabal and Sánchez, 2020). However, open repositories with extensive image catalogs and relatively long time frames have allowed the documentation of events that were not captured by more precise but localized methods in the days following the event, such as aerial photographs acquired from UAVs (Giordan et al., 2015; Guzzetti et al., 2012). In particular, Sentinel-2 allows the comparison of pre- and post-event composites over extensive areas, making it possible to map a complete inventory, although with a limitation on the minimum size of the landslides that can be detected (Notti et al., 2023).

The compilation of these events in the Colombian Andes offers an opportunity to identify patterns in their occurrence amidst the continuing urbanization of rural areas (Sánchez-Rodríguez and Correa, 2022), often without prior planning regarding the hazard conditions of the site (Nieto et al., 2025; Ozturk et al., 2022). The fact that at least one such event has been documented every year over the past decade, and up to three in a single year, raises questions about their spatiotemporal occurrence. In this study, we compile and analyze 13 landslide events that occurred in the Colombian Andes between 2015 and 2025, comprising 8,088 mapped landslides. We characterize these events using morphometric and lithological variables, landslide size distributions, spatial density, slope-aspect relationships, rainfall conditions, and multivariate analyses. The main objectives are to (1) identify recurrent geomorphological and geological characteristics associated with the events, (2) characterize differences in their spatial concentration and orientation according to the triggering mechanism, (3) examine the short-term and antecedent rainfall preceding each event and its relation to ENSO conditions, and (4) evaluate the relative contribution of morphometric variables to differences within and among inventories. By compiling these inventories into an open regional dataset, this study provides a basis for comparing multiple-occurrence landslide events in the Colombian Andes and for future research on the processes that influence them.

2 Study area and events

The study area is located on the Colombian Andes, a region extending approximately 1200 km from northern Ecuador to the Caribbean plains. This section of the Andes is divided into three mountain ranges, where most of the population and socioeconomic activities are concentrated. The elevation difference across the Andean landscape ranges from 500 meters in

the lower piedmont areas to almost 5000 meters in the snow-capped volcanoes of the central cordillera. This mountain evolution is the result of two simultaneous processes: first, the tropical climate, influenced by the passage of the Intertropical Convergence Zone (ITCZ) and the Chocó low-level jet stream (Bedoya-Soto et al., 2019; Mesa et al., 2000; Poveda, 2004). Second, geodynamic activity at tectonic plate boundaries, where the convergence of the Nazca oceanic plate with the South American continental plate influences the tectonic uplift and exhumation rate (Pérez-Consuegra et al., 2021; Restrepo-Moreno et al., 2019; Noriega-Londoño et al., 2020). The morphometric characteristics, rainfall patterns, and lithological properties resulting from these interactions create a scenario prone to landslides.

This research compiles the landslide events in the decade from 2015 to 2025 (Figure 1). The first panel shows the location of the events in the Colombian Andes. Panels (1)-(13) show the mapped landslide polygons of each inventory over a hillshade derived from the ALOS PALSAR DEM (12.5 m). Table 1 shows the data of each event. The first recorded event occurred in Salgar (2015), triggered by a 160 mm rainfall event, which resulted in 108 landslides that evolved into a debris flood, causing over 100 fatalities (Hidalgo and Vega, 2021). Two years later, in 2017, another debris flood occurred in the city of Mocoa (1,082 landslides triggered by a 130 mm/3 hr rainfall event). As in Salgar, most of the losses in Mocoa were caused by the propagation of the material in the channels; official records report 333 fatalities, 398 injured, and 71 people missing (Prada-Sarmiento et al., 2019b; García-Delgado et al., 2019). Figure 2 shows landslides in the Mocoa event, illustrating the typical morphology of the process in the northern Andean narrow and steep valleys. These first two events account for almost all of the most severe impacts and significantly highlighted the severity of hydrometeorological hazards. Following these disasters, numerous efforts were undertaken to develop plans for assessing susceptibility, hazard, and risk of landslides, flash floods, and debris flow (Rodríguez et al., 2017; Servicio Geológico Colombiano, 2021). However, further events have occurred, along with the resulting damage. Then, an earthquake of 6.0 magnitude struck the eastern foothills of the Eastern Cordillera of Colombia in December 2019 at a depth of approximately 13 $\pm$ 2.9 km, triggering 838 landslides (García-Delgado and Contreras, 2021). In 2019 and 2020, four events occurred in the department of Antioquia, Colombia (Jericó, 2019; Anorí, 2020; Yali, 2020; Dabeiba, 2020). The latter two caused the greatest losses. Yali recorded 4,068 landslides, the landslide event with the highest number of events and affected area recorded to date in the Colombian Andes. The Dabeiba 2020 event, with far fewer landslides but in a more densely populated area, resulted in the

loss of 5 lives. From 2021 to 2024, 5 more events occurred in the same department, with an average of approximately 200 landslides and smaller affected areas (Santo Domingo, 2021; Anori, 2023; Girardota, 2023; Cerro Bravo, 2024; and Altavista, 2025). The most recent event was Paratebueno in 2025, close to the border of the Llanos Basin and Andean regions, triggered by a magnitude 6.4 earthquake at a depth of 9 km, producing a landslide of more than 100 hectares and 284 smaller landslides.

Table 1: Landslide events compiled in this study

#	Event	Municipality (Dept.)	Date	Lat. (°N)	Lon. (°W)	N	Deaths / missing	Trigger	Dominant lithology	Source
1	Salgar 2015	Salgar (ANT)	2015-05-18	6.00	76.09	108	104 / 10	Rainfall	Clastic sedimentary	Marín et al., 2021
2	Mocoa 2017	Mocoa (PUT)	2017-03-31	1.17	76.67	1082	333 / 71	Rainfall	Clastic sed./intrusive	Prada-Sarmiento et al., 2019a
3	Mesetas 2019	Mesetas (MET)	2019-12-24	3.50	74.15	838	–	Earthquake	Low-grade metasedimentary	García-Delgado et al., 2019
4	Anorí 2020	Anorí (ANT)	2020-05-21	7.19	75.28	266	–	Rainfall	Foliated metamorphic	Palacio Cordoba, 2023
5	Yalí 2020	Yalí (ANT)	2020-07-05	6.71	74.72	4068	1 / 0	Rainfall	Foliated metamorphic	Palacio Cordoba, 2023
6	Jericó 2019	Jericó (ANT)	2019-11-04	5.80	75.79	26	–	Rainfall	Extrusive igneous	
7	Dabeiba 2020	Dabeiba (ANT)	2020-11-13	6.94	76.26	135	5 / 0	Rainfall	Extrusive igneous	Aristizábal et al., 2025
8	St. Domingo 2021	Santo Domingo (ANT)	2021-05-31	6.49	75.11	223	–	Rainfall	Intrusive igneous	Palacio Cordoba, 2023
9	Anorí 2023	Anorí (ANT)	2023-07-17	7.08	75.13	321	–	Rainfall	Foliated metamorphic	Palacio Cordoba, 2023
10	Girardota 2023	Girardota (ANT)	2023-05-28	6.41	75.45	327	–	Rainfall	Intrusive igneous	
11	Cerro Bravo 2024	Fredonia (ANT)	2024-06-25	5.94	75.71	123	2 / 3	Rainfall	Intrusive igneous	
12	Altavista 2025	Medellín (ANT)	2025-04-29	6.22	75.64	287	2 / 0	Rainfall	Intrusive igneous	
13	Paratebueno 2025	Paratebueno (CUN)	2025-06-08	4.40	73.30	285	–	Earthquake	Clastic sedimentary	
			Total			**8088**	**447 / 84**			

ANT: Antioquia; PUT: Putumayo; MET: Meta; CUN: Cundinamarca. N: number of mapped landslides. Dashes indicate no reported casualties.

3 Data and methods

The methodology of this study consists of four steps to explore the geomorphological and triggering characteristics of the thirteen collected events across the Colombian Andes Cordillera during one decade. First, we gathered the available inventories; most of them were not digital available because they were just reported as an event with a specific date on the news or a formal thesis instead of an official inventory. For this reason, most of them were created through manual

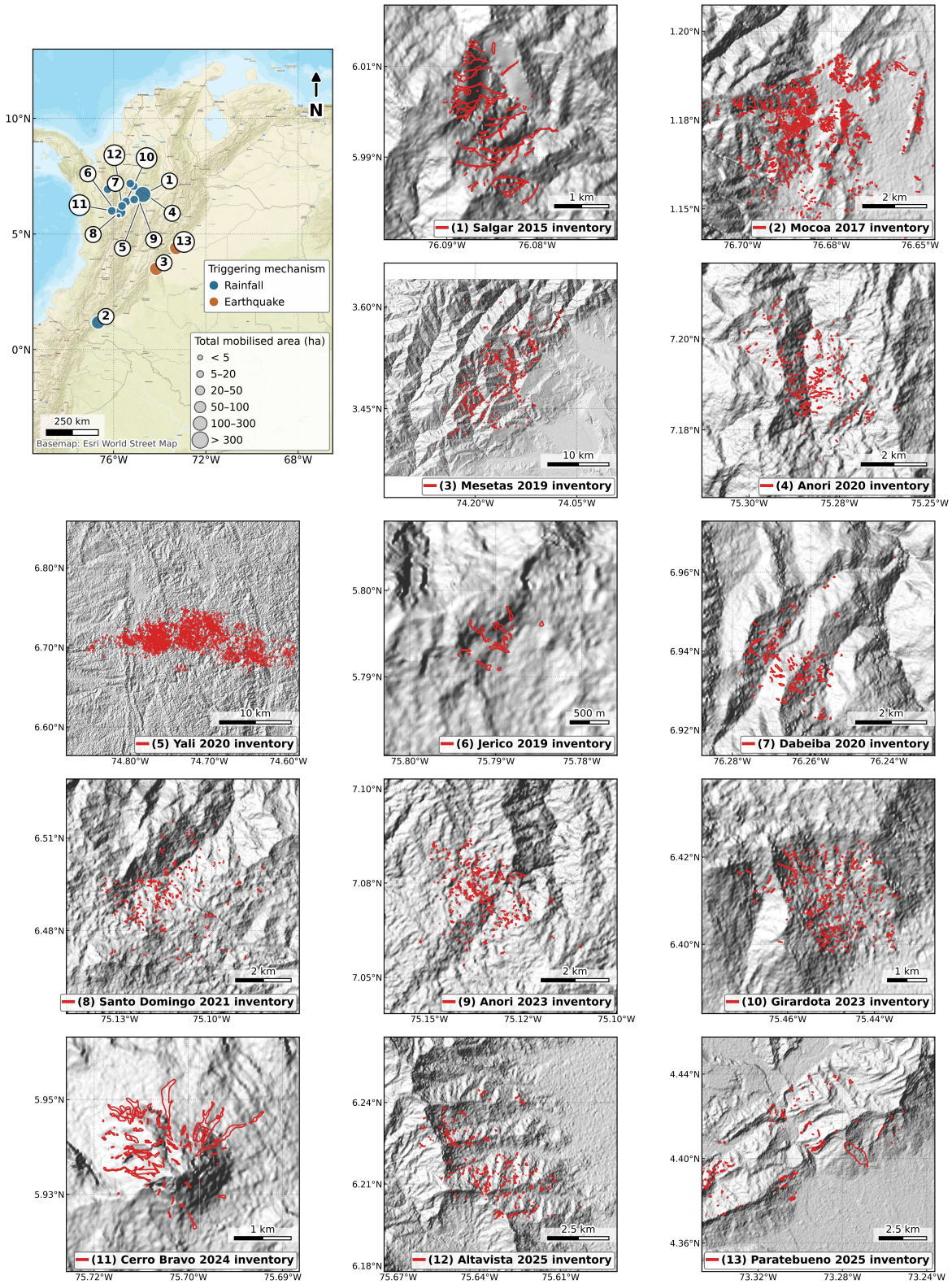


Figure 1: Location and mapped extent of the 13 events compiled in this study.



Figure 2: Aerial photographs illustrating the typical morphology of landslides in northern Andes: shallow translational landslides and debris flows developed on steep slopes. Photographs: Corpoamazonia, Mocoa, 2017.

delineation over Sentinel-2 images after evaluation of pre- and post-event mosaics. Then, we followed a morphological description of the events through terrain parameters and an exploration of the triggering factor using satellite rainfall data. Finally, we explored all events through statistical tools using principal component analysis.

3.1 Landslide inventory compilation

The events studied in this work correspond to the period from 2015 to 2025, starting with the event of Salgar in May 2015 and finalizing with the event of Paratebueno in July 2025. During this starting period that cover this study, Sentinel-2 was releasing satellite images from diverse parts of the world, but in the case of some areas of Colombia, it was not available. For the three initial events, we used secondary information on previous events that were widely studied trhough the years: Salgar, 2015 (Velásquez et al., 2020; Marín et al., 2021; Aristizábal-Giraldo and Ruiz-Vásquez, 2023; Gómez Cardona et al., 2025); Mocoa, 2017 (Prada-Sarmiento et al., 2019a; García-Delgado et al., 2019), Mesetas, 2019 (García-Delgado and Contreras, 2021) and Dabeiba, 2020 (Aristizábal et al., 2025). The next nine events were created through manual delineation over Sentinel-2 images. These events, at the same time were less noted due to the less amount of damage that they caused to the human lives, infrastructure and ecosystems.

Google Earth Engine was used to create the mosaics of pre- and post-event images of the reported date for each event. We used a window of three months before and three months after the event to find a suitable mosaic of images that represent each study area free of clouds; this is a particular problem during the rainy season of the year or during constant days and weeks of precipitation previous to the event. In the Figure 4, three examples are presented. (a) and

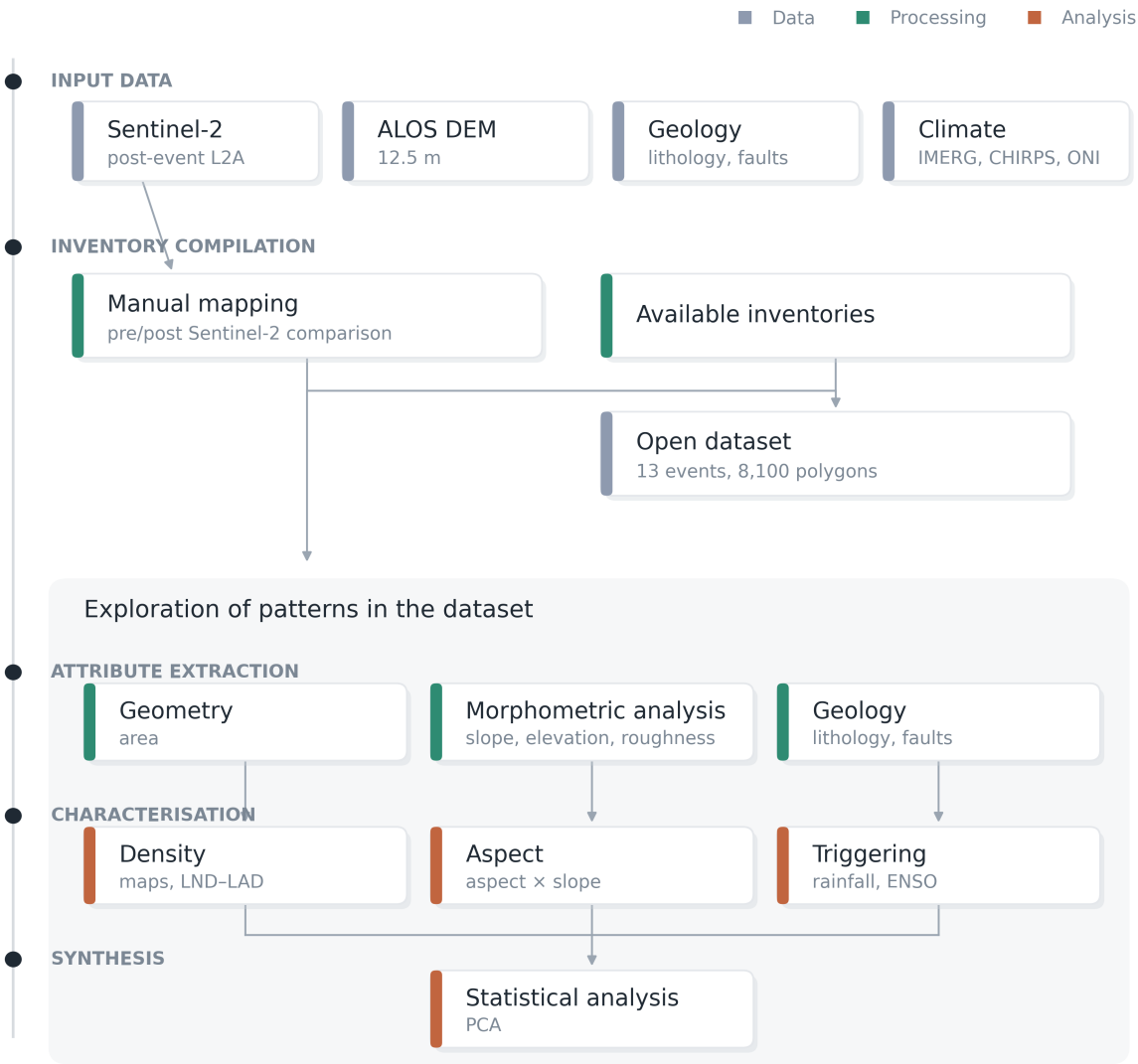


Figure 3: Workflow of the study.

(b) illustrate the change detection in a steep hill covered by dense Andean forest, 123 landslides were mapped. (c) and (d) show the change in a mosaic of forest and grass in the limits of the Andean Cordillera and Llanos basin, the number of landslides found in this area was 285. (e) and (f) show the change in a wide area in the municipality of Yali, Antioquia; 4068 landslides were manually mapped for this event. After selecting the images and visual inspection of the quality of landslide shapes presented in the images, we start to delineate the landslides for each event. The delineation of the polygons was performed using Q-GIS v3.40 software and supported with ALOS PALSAR DEM 12.5 resolution using hillshade and slope attributes. The inventory of the events is available for further works, and it can be found in this repository: LINK.

3.2 Terrain attribution and geology data

Multiple layers were generated from the available Alos Palsar DEM 12.5 m resolution. Some DEMs with more optimal resolution were available for specific sites, but to maintain consistency among study areas and avoid biases in the analysis, we opt to use the same DEM resolution for all events. The layers generated were Slope, Terrain Ruggedness Index (TRI), Distance to Drainage, Elevation, Topographic Wetness Index (TWI), Flow Accumulation, and Height Above Nearest Drainage (HAND). One important morphological variable considered in this study was the area of the landslides within each inventory; it was explored using statistical distributions.

The layer of lithological units was extracted from the maps of geology in a scale of 1:100,000, freely available by the Geological Service of Colombia (SGC). This information includes the name of rocks, composition, and age. In this study, we used the general composition of the rock to simplify the analysis, assuming that the soil in the landslide displacement was developed from this lithological unit. From the same source, we found the data about faults to develop the distance-to-faults layer.

From each set of polygons of the events, the data were extracted from terrain variables and geological maps. Additionally, we explored each catchment where the landslide event was present, extracting the same information of morphometrical variables to constrast against the information extracted from polygons of landslides. So, instead of extracting the information of landslides alone, this was used on purpose to understand if there are patterns between specific landslide areas and the local terrain where landslides did not occur.

Two additional variables were included in the exploration of patterns: density and aspect. Density was evaluated individually for each area and related to the influence of lithological units.

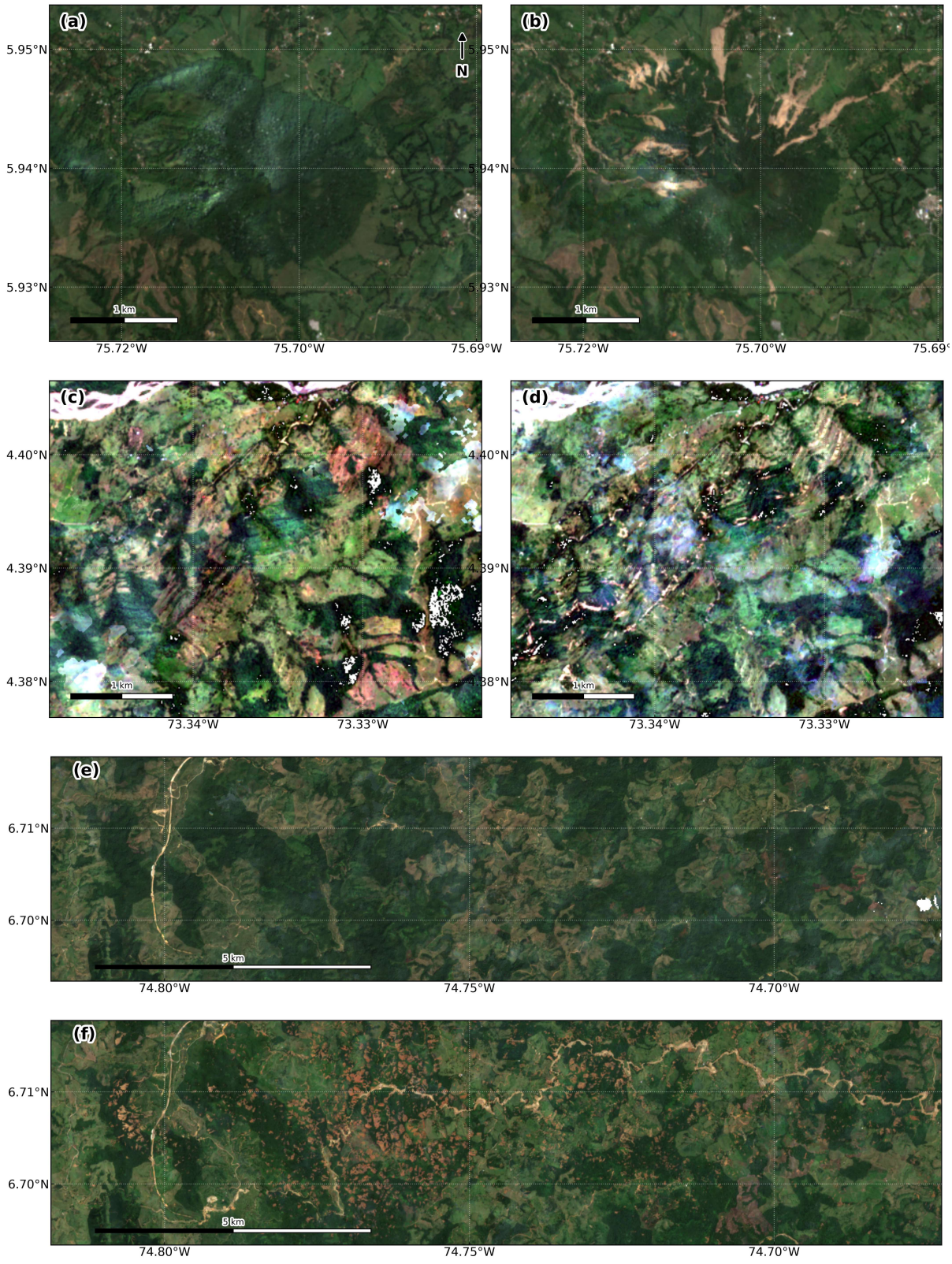


Figure 4: Pre- and post-event Sentinel-2 composites for three representative inventories: (a) pre-event Cerro Bravo 2024; (b) post-event Cerro Bravo 2024; (c) pre-event Paratebueno 2025; (d) post-event Paratebueno 2025; (e) pre-event Yalí 2020; and (f) post-event Yalí 2020.

The evaluation analyzes the spatial concentration of landslides using a moving-window density approach. For each inventory, the landslide polygons were projected to a local UTM coordinate system, and a representative point was assigned to each polygon. These points were used to construct a regular 100 m × 100 m grid covering the inventory and a 3 km buffer around its extent. A circular moving window with a radius of 1 km was applied to the grid. Within each window, the number of landslides was counted and normalized by the area of the circular window to obtain the Landslide Number Density (LND), expressed as the number of landslides per km^2:

$$\mathrm{LND}(x, y) = \frac{N_r(x, y)}{A_r} \tag{1}$$

where $N_r(x, y)$ is the number of landslide representative points within the circular window centered at (x, y), and A_r is the area of the 1 km radius moving window. In parallel, the total area occupied by landslides within the same window was normalized by the window area to obtain the Landslide Area Density (LAD), expressed as the percentage of terrain affected by landslides:

$$\mathrm{LAD}(x, y) = \frac{\sum_{i=1}^{N_r} A_i}{A_r} \times 100 \tag{2}$$

where A_i represents the area of the i-th landslide intersecting the moving window and N_r is the number of landslides within the window.

The resulting density surfaces were subsequently sampled at the representative point of each landslide to obtain a local LND and LAD value for every polygon. For each inventory, the median local LND was used as a measure of the typical landslide concentration, while the corresponding LAD values were used to characterize the proportion of terrain affected by landslides. These metrics were used to compare the spatial concentration of landslides among the 13 inventories independently of the extent of the surrounding analysis area. The median local LND was then plotted against the median local LAD for each inventory to characterize differences in landslide concentration and affected area.

On the other hand, the variable aspect was evaluated by triggering factor and was contrasted against the variable slope. This analysis was conducted to evaluate whether the spatial distribution of landslides across slope aspects differed from the distribution of the available terrain within the catchments of each event. At the same time, the effect of slope was considered to assess whether the spatial distribution of landslides was more strongly associated with slope or aspect.

Finally, the analysis discriminated the representation of these relationships between rainfall- and earthquake-triggered inventories.

For this analysis, the aspect and slope were calculated for each DEM pixel within the study areas. The aspect was divided into 16 directional sectors of 22.5°, while slope was classified into eight bands ranging from 5° to 45°. Since the Alos Palsar DEM was used, slope values above 45° were uncommon; for this reason, 45° was used as the upper limit of the analysis. Each pixel was assigned to a combination of aspect sector and slope band. The pixels were classified as landslide or terrain according to their spatial intersection with the corresponding landslide inventories.

For each aspect–slope combination, the proportion of landslide pixels was calculated as:

$$P_{\mathrm{LS}}(a,s) = \frac{N_{\mathrm{LS}}(a,s)}{N_{\mathrm{LS}}} \tag{3}$$

where $N_{\mathrm{LS}}(a,s)$ is the number of landslide pixels within aspect sector a and slope band s, and N_{LS} is the total number of landslide pixels in the corresponding group of inventories. Similarly, the proportion of available terrain within each aspect–slope combination was calculated as:

$$P_{\mathrm{T}}(a,s) = \frac{N_{\mathrm{T}}(a,s)}{N_{\mathrm{T}}} \tag{4}$$

where $N_{\mathrm{T}}(a,s)$ represents the number of terrain pixels within the corresponding aspect sector and slope band, and N_{T} is the total number of terrain pixels considered.

The relative representation of landslides within each aspect–slope combination was then calculated as the ratio between the landslide and terrain proportions:

$$R(a,s) = \frac{P_{\mathrm{LS}}(a,s)}{P_{\mathrm{T}}(a,s)} \tag{5}$$

where $R(a,s) = 1$ indicates that the proportion of landslide pixels is equivalent to the proportion of available terrain for a given aspect and slope combination. Values greater than one indicate a higher representation of landslides relative to the available terrain, whereas values lower than one indicate a lower representation.

The resulting ratios were represented in polar diagrams, with the angular coordinate corresponding to aspect and the radial coordinate corresponding to slope. The colour scale was centred at $R = 1$ to facilitate the comparison between the observed landslide distribution and the available terrain. The analysis was performed separately for all inventories combined, rainfall-triggered inventories, and earthquake-triggered inventories. The rainfall-triggered group included the

inventories classified as rainfall-induced, whereas the earthquake-triggered group included the Mesetas 2019 and Paratebueno 2025 inventories.

3.3 Rainfall context

We used satellite rainfall data instead of gauge precipitation. This type of data was used due to the lack of stations around the study areas. Most of the events occurred in remote areas where the interest in measuring precipitation is considerably reduced by the priorities of governmental and private institutions.

The data were extracted from two sources, CHIRPS v2 and GPM IMERG v07 daily rainfall data. CHIRPS provides quasi-global precipitation estimates at a spatial resolution of 0.05° (approximately 5.5 km at the Equator), with daily data available from 1981 to the present. GPM IMERG v07 provides global precipitation estimates at a spatial resolution of 0.1° (approximately 10 km at the Equator) and a temporal resolution of 30 minutes, with data available from 1998 to the present. GPM IMERG hourly rainfall data was transformed into daily data for the purpose of the study. The raster information was obtained from Google Earth Engine, and the calculation was performed directly on the platform. First, the exact day of the event was identified. Second, we extract the triggering rainfall and antecedent rainfall based on this date. The antecedent rainfall is defined as the total rainfall accumulated over the 90 days before the event. Triggering rainfall is defined as the rainfall during the day of the event; also, 3 days and 5 days were included before the triggering day to contrast with antecedent rainfall.

To assess the temporal occurrence of the events during the last decade, we use the variability due to the changes caused by ENSO. The conditions of precipitation can dramatically change depending on this. For that, we create a chronology from 2015 to 2025 with the Oceanic Niño Index (ONI) and the date of occurrence of the event. In addition to this, we included the earthquake-triggered factor in this analysis. Earthquake-triggered landslides can be influenced by the amount of rainfall present in the soil profile before the earthquake.

3.4 Statistical analysis

As the last step of the methodology, we performed a Principal Component Analysis (PCA) to obtain a hierarchical classification of the inventories in the PCA space. For this analysis, we used the morphometric variables analyzed in the previous data exploration. The analysis was conducted at the individual landslide-polygon level, using polygon area, relative elevation, slope,

distance to drainage, distance to faults, roughness, local landslide density, HAND, and flow accumulation as input variables. Prior to the PCA, area, distance to drainage, flow accumulation, and distance to faults were log-transformed. Relative elevation was expressed as a percentile within each study area to allow comparison among regions with different absolute elevations.

Variables were standardized using the StandardScaler transformation before performing the PCA. Redundant variables identified during a correlation analysis were excluded from the analysis, including the topographic wetness index (TWI) and aspect. The PCA was performed using the complete set of landslide polygons from the 13 inventories. To characterize the distribution of each inventory within this space, the centroid of each event was calculated from the projected landslide polygons.

We evaluate the contribution of the input variables using an intraclass correlation analysis (ICC) that was performed for each morphometric variable. This analysis addressed whether differences in the values of a given variable were mainly associated with differences between inventories or with the variability among individual landslides within the same inventory. In this framework, the total variability of each variable was expressed as the sum of the between-inventory and within-inventory components:

$$\sigma^2_{\text{total}} = \sigma^2_{\text{between}} + \sigma^2_{\text{within}} \tag{6}$$

The ICC was then calculated as the proportion of the total variance associated with differences among inventories:

$$ICC = \frac{\sigma^2_{\text{between}}}{\sigma^2_{\text{between}} + \sigma^2_{\text{within}}} \tag{7}$$

Additionally, a PCA biplot was generated to characterize the contribution of the input variables to the distribution of inventories in the principal component space. The loadings of the original variables were projected onto the PC1–PC2 space together with the inventory-specific centroids. This allowed the relationships between the morphometric variables and the position of each inventory in the PCA space to be evaluated.

4 Results

The collected and mapped dataset of landslide inventories included 8088 polygons. We describe the attributes of the polygons of these 13 events based on a spatial analysis and exploration, including the terrain characteristics, lithological setting, spatial concentration and orientation, rainfall conditions, and multivariate analysis.

4.1 Terrain characteristics

We analyze the size distribution of the events, where 55% of the total area of landslides is under 5000 m² and corresponds to 93% of total landslides. The rest of 45% of total area landslide is over 5000 m² and corresponds to 7% of landslides (Fig. 5a). The class between 1,000 and 5,000 m² dominated the analysis in terms of count, with 33% of the polygons and 39% of the mobilized area, so the size distribution of the inventory is controlled by intermediate landslides and second by the small landslides. On the opposite side, landslides over 10,000 m2 are only 2% of the polygons but account for 26% of the total area.

The size distribution was discriminated by event, where the two earthquake-triggered landslides show two notable aspects: Mesetas 2019 is the largest inventory by size with the highest median, while Paratebueno 2025 has the largest landslide registered with approximately 100 hectares of terrain affected by one landslide. These two events also show different distributions of landslide sizes. Mesetas 2019 presents a relatively high central tendency and a broad distribution, while Paratebueno 2025 presents a more moderate median but an extreme upper tail associated with the largest landslide of the dataset. In terms of rainfall-triggered events, the largest median landslide size was Cerro Bravo, an event occurring in a steep hill covered by an Andean forest where huge hillslope debris flow was affecting the whole hill and mobilizing as a debris flow downslope. Cerro Bravo also presents a relatively large central tendency compared with most of the rainfall-triggered events. For example, Girardota 2023, Anori 2023, and Altavista 2025 are more concentrated toward smaller landslide sizes, whereas Salgar 2015, Mocoa 2017, and Yali 2020 show a broader distribution.

Figure 6 illustrates the morphometric setting; eight variables were included in this analysis, and two violin plots were created to distinguish landslides and non-landslide terrain of the catchment where the events occurred. This distinction was applied for all variables. Colored circles show the median values at landslide locations for every event; the same representation with

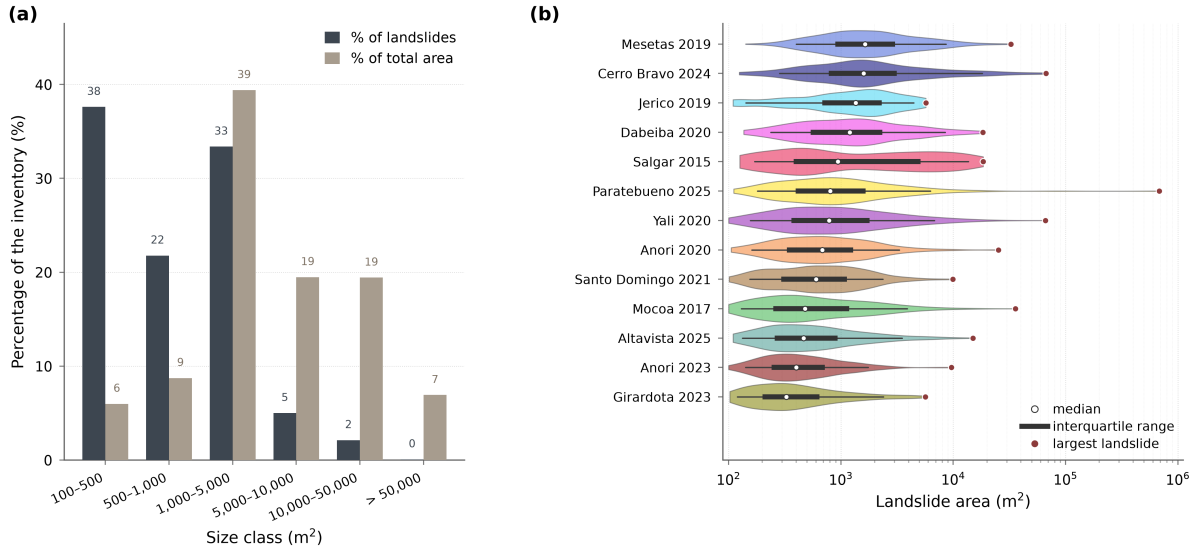


Figure 5: Landslide size statistics. (a) Percentage of landslides (blue) and of total mapped area (orange) contained in each size class. (b) Distribution of landslide area per inventory, ordered by decreasing median

colored circles is applied to median values in non-landslide terrain. On top of the figure, elevation shows similarities between circles of two categories, with a difference of only +46.8 m over a range going from 500 to 3000 m. The slope variable shows a marked difference; non-landslide terrain has lower median values than the landslide events, with a difference of +6.4 degrees. This is a consistent pattern across the 13 events, with landslide locations generally associated with steeper terrain than the surrounding non-landslide terrain. Distance to drainage has a marked pattern where all landslide events are taking the lowest values of the distance, while the non-landslide terrain has the opposite. Among the analyzed variables, distance to drainage shows one of the clearest separations between the two categories, a difference of −125.7 m, with landslide locations consistently closer to drainage networks. A similar trend is noted in roughness (TRI) and flow accumulation variables; landslide events have higher median values, with +1.2 m and +0.17 $\log_{10}$ m^2, respectively. Distance to faults and HAND have similar values between the two categories, with slightly higher landslide events median values on the right side of the HAND variable. HAND also presents a considerable variation between events, with no clear common value separating landslide and non-landslide terrain. Similarly, distance to faults shows a high variability between events and does not present a consistent separation between the two categories.

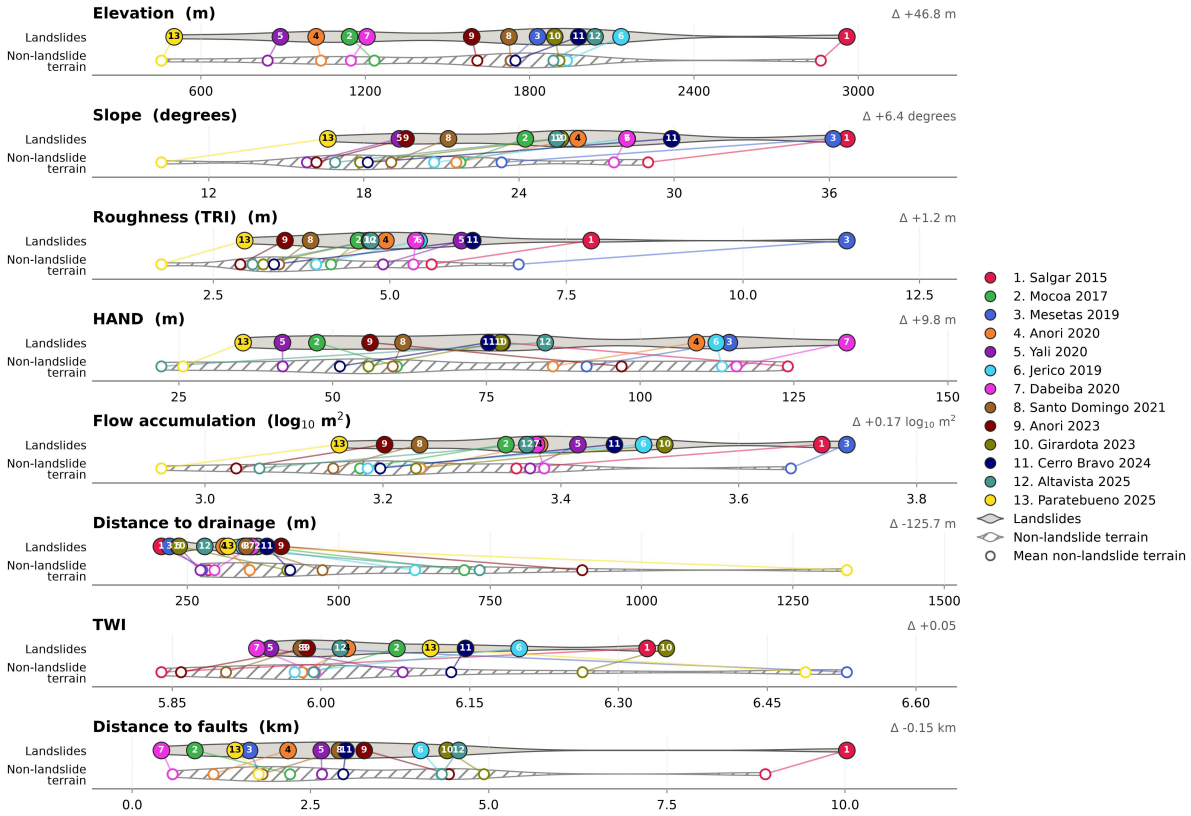


Figure 6: Morphometric setting of the landslides compared with the catchment terrain where the events occurred. For each variable, colored circles show the median value at landslide locations for every event.

4.2 Lithological setting

The lithological composition of the events is illustrated in Fig. 7a. Most of the events are composed of igneous rocks. Four events are dominated by intrusive igneous rocks (Santo Domingo 2021, Girardota 2023, Cerro Bravo 2024, and Altavista 2025) and two by extrusive igneous rocks (Jerico 2019 and Dabeiba 2020). The remaining events are mostly distributed in clastic sedimentary rocks and foliated metamorphic rocks: four are dominated by clastic sedimentary rocks (Salgar 2015, Mocoa 2017, Mesetas 2019, and Paratebueno 2025), and three by foliated metamorphic rocks (Anori 2020, Yali 2020, and Anori 2023). Fig. 7b shows the soil grain size, where around 70% of the events are coarse-grained. Additionally, we compare the landslide area discriminated by the lithological group, as is shown in Fig. 8a. Chemical sedimentary rocks and metasedimentary rocks, followed by extrusive igneous rocks, are the groups with the highest sizes of landslides; this can be aggregated by the implications of the sizes of the Mesetas 2019 event, where this event shows the highest median areas of landslides and is the unique event that reports these types of lithologies. The landslide areas discriminated by soil grain size are shown in Fig. 8b, where fine-grain soils have a slightly higher median than coarse-grain soils, with

a difference under half of an order of magnitude and interquartile ranges that overlap almost completely. The largest landslide of the whole dataset, the one reported in Paratebueno 2025, is located on coarse-grain soils and on clastic sedimentary rocks.

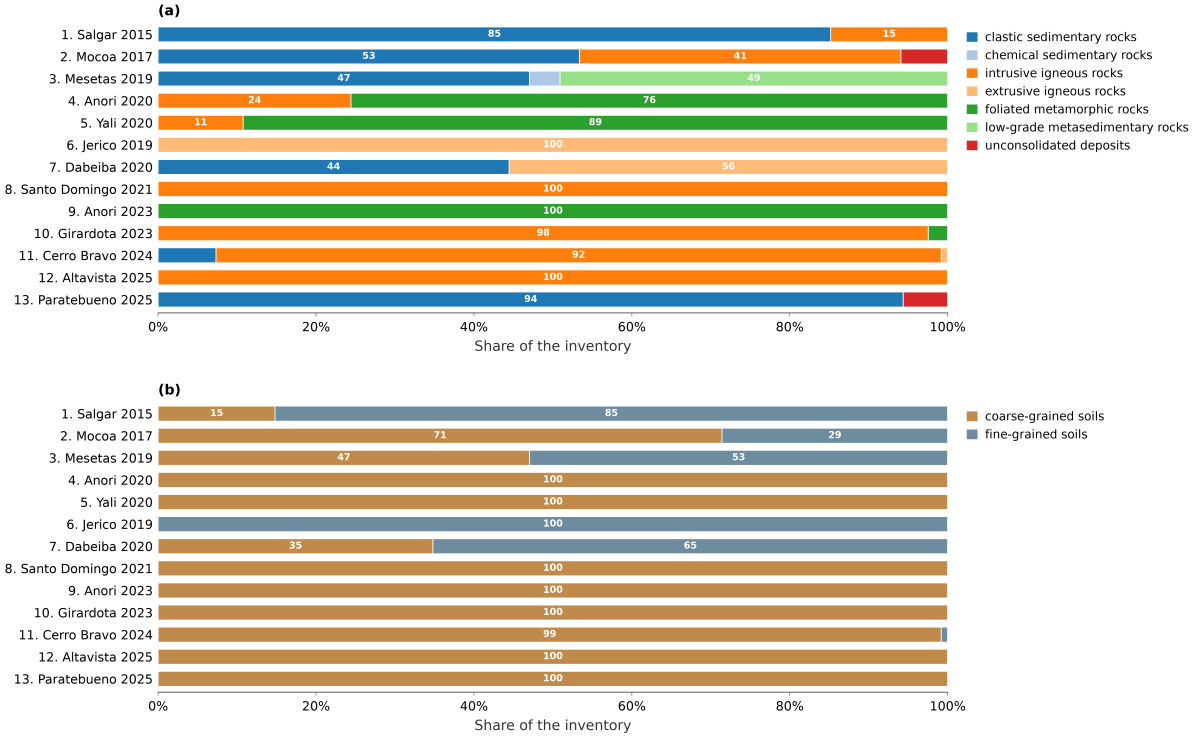


Figure 7: Lithological and soil composition of each inventory. (a) Share of each inventory's landslides on each lithological group; (b) Share of each inventory's landslides by soil grain size.

4.3 Spatial concentration and orientation

An analysis of local density was carried out in the study areas. The highest concentrations were present in Yali 2020 and Mocoa 2017, as shown in Fig. 9. Five cores of concentrations, over 100 landslides per km^2, were identified in Yali, 2020, while one core was identified in Mocoa 2017. In Altavista 2025 a core with a concentration of over 20 landslides per km^2 affected an area of 5 km in length. Earthquake-triggered landslides in the figure (Mesetas 2019 and Paratebueno 2025) presented a different pattern shape, where the landslides are spread in a medium and small core concentration disconnected from a unique elongated shape, as the rainfall-triggered landslides. Figure 10 shows the median area density, which can be seen as the percentage of affected area versus median landslide number density. The grey isolines on the right of the figure represent the mean landslide size; these lines show how events with different mean landslide sizes obtained similar values of median local density. Each event has an error bar, which spans the interquartile range of each inventory. As the figure shows, high concentrations of landslides and affected areas

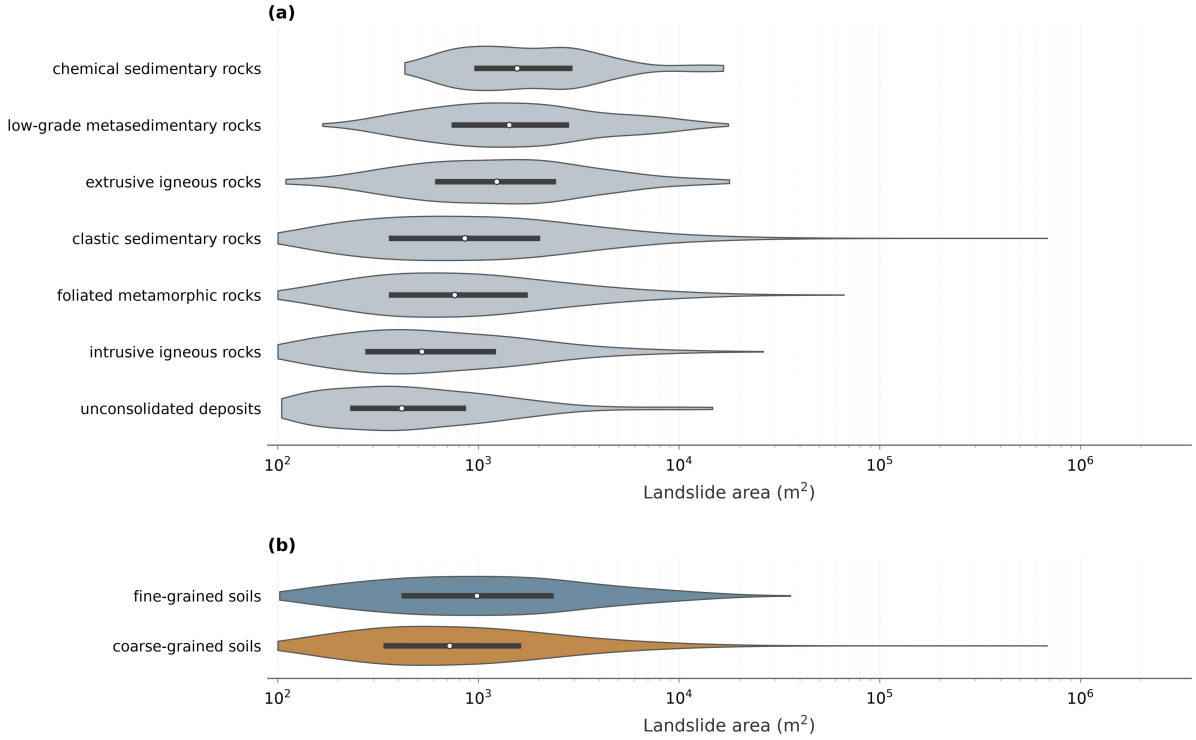


Figure 8: Landslide size distribution by lithological group and inferred soil grain size. (a) Distribution of landslide areas over each lithological group; (b) the same, grouped by the soil grain size.

were Mocoa 2017 and Yali 2020, followed by events like Cerro Bravo 2024, Anori 2023, Girardota 2023, and Anori 2020. Earthquake-triggered landslides, Mesetas 2019 and Paratebueno 2025, and small rainfall-triggered events Jerico 2019, are the events with the lowest median values of landslide density.

The preferred orientation of landslides was evaluated using a circular heatmap (Figure 11), where the angular coordinate represents aspect and the radial coordinate represents slope. Values above 1 (reddish colors) indicate a higher relative representation of landslides, whereas values below 1 (blue colors) indicate a higher representation of non-landslide terrain. Three analyses were carried out considering all events, rainfall-triggered events, and earthquake-triggered events. Across the three analyses, the highest landslide preference values are concentrated in the outermost rings, corresponding to slopes greater than 40°. This pattern indicates that slope has a stronger and more consistent relationship with landslide occurrence than aspect, with landslides being preferentially located on the steepest slopes. However, differences in aspect distribution are also observed between the three datasets. For all events (Fig. 11a), higher preference values are more frequent in the eastern sector, particularly where several values exceed 2, whereas lower values are concentrated mainly toward the west. For rainfall-triggered landslides (Fig. 11b), the overall preference values are lower and the concentration toward the steepest slopes is less pronounced

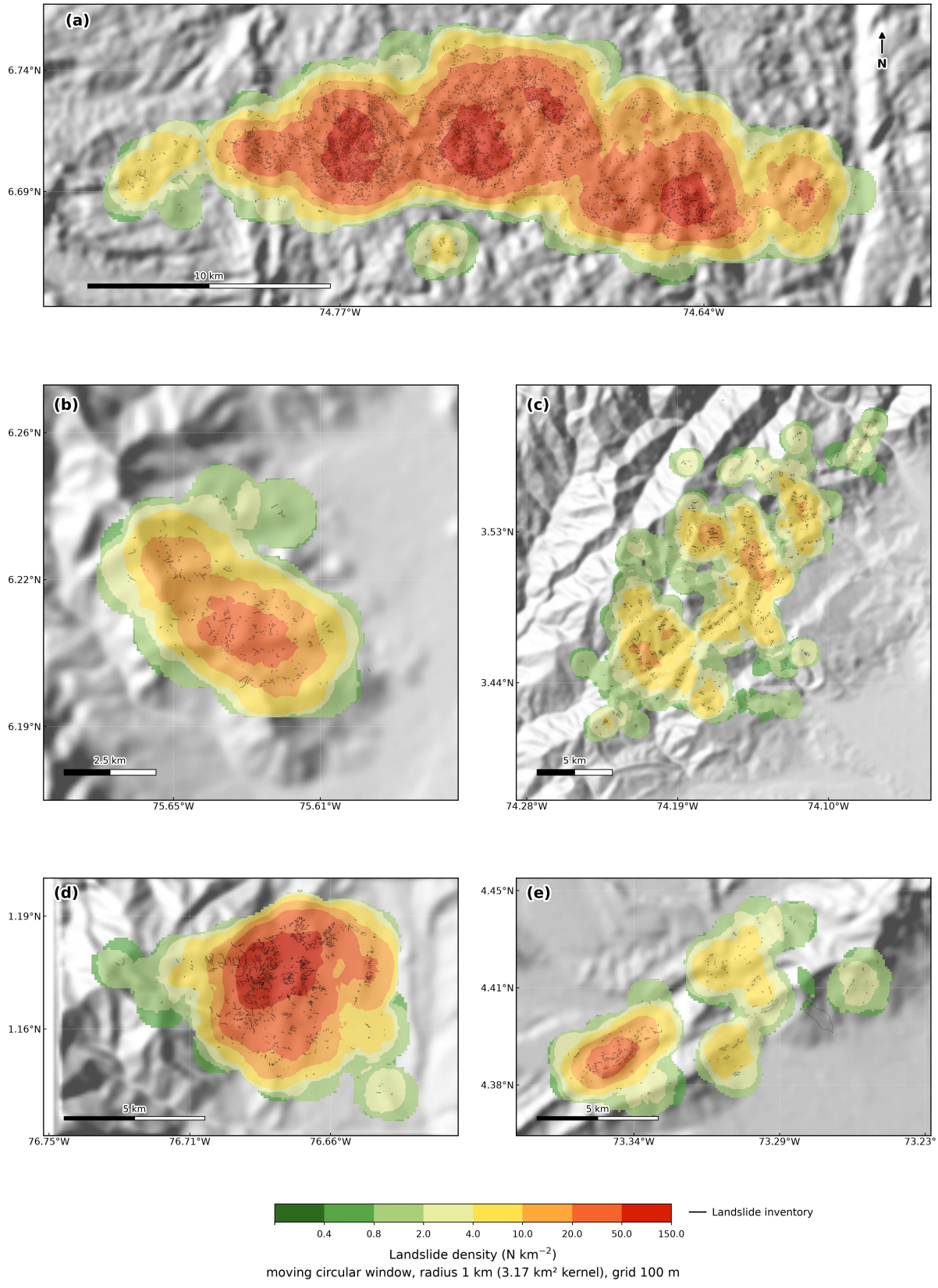


Figure 9: Spatial density of landslides for five representative inventories: (a) Yalí 2020, (b) Altavista 2025, (c) Mesetas 2019, (d) Mocoa 2017, and (e) Paratebueno 2025.

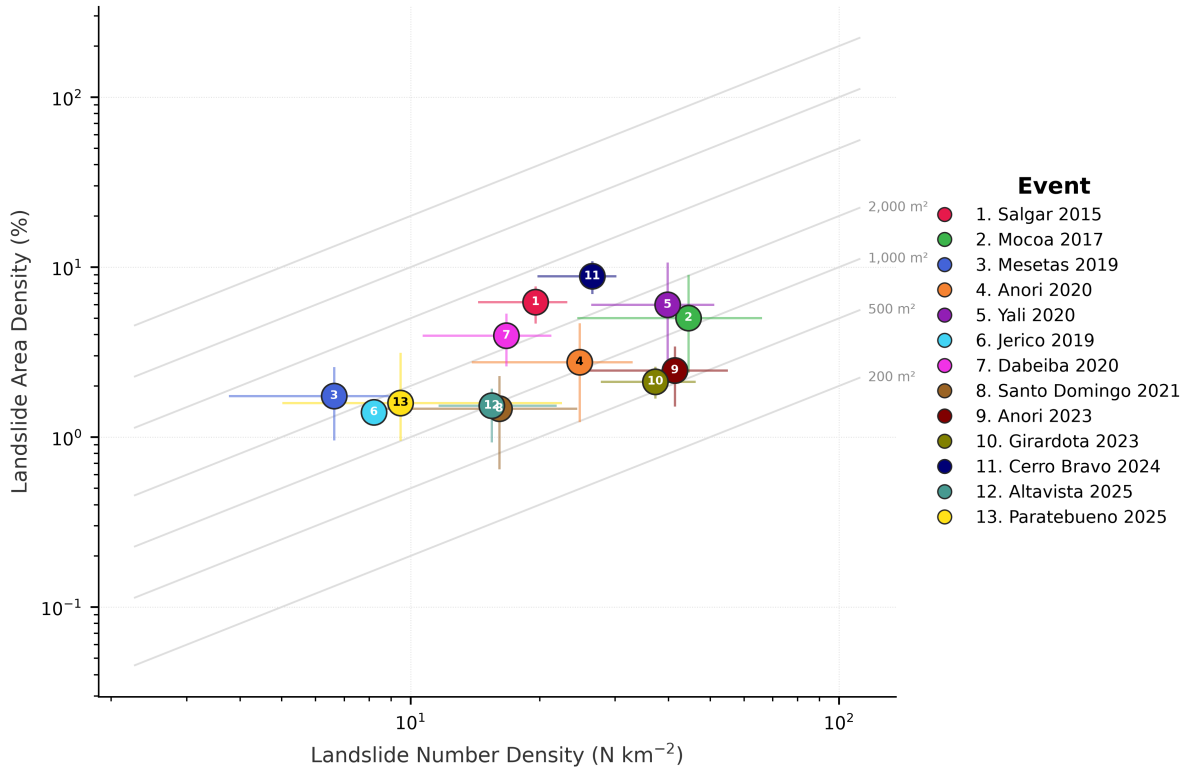


Figure 10: Median landslide area density versus median landslide count density evaluated at landslide locations, using a circular window of 1 km radius.

than for the complete inventory. Nevertheless, the outermost rings still show higher values than the lower-slope rings. The western sector again presents the lowest preference values, while the eastern and southeastern sectors show relatively higher values. The earthquake-triggered landslides (Fig. 11c) show a more pronounced directional pattern. Higher preference values are distributed across three of the four main sectors, with the strongest values occurring at moderate to steep slopes. In this case, the increase in preference with slope becomes more evident from approximately 30° upward. In contrast, the NW sector shows a marked decrease in landslide preference, with predominantly low values across several slope ranges.

4.4 Rainfall conditions

Antecedent rainfall was reconstructed for the 90 days preceding each event from two independent products, CHIRPS and IMERG V07 (Fig. 12). Daily totals are shown as mirrored bars, CHIRPS upwards and IMERG downwards, and the diagonal curves give the cumulative rainfall for the two types of satellite data. In most of the events, IMERG data has the highest cumulative values in a range from 600 mm to 1250 mm. The difference of the two types of data is approximately 100 to 200 mm for cumulative rainfall in each event. On the other hand, the rain during the

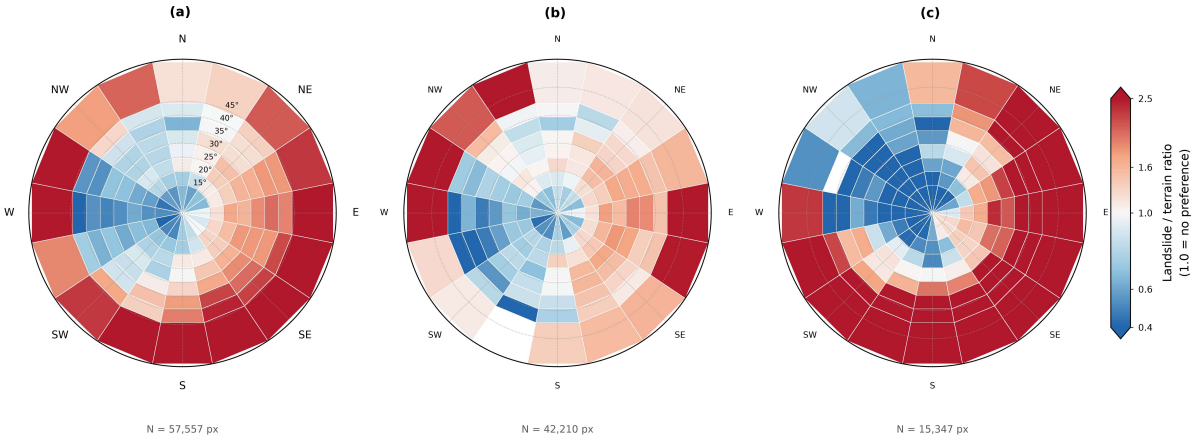


Figure 11: Ratio between the observed landslide and the non-landslide terrain frequency for each aspect—slope class: (a) all events, (b) rainfall-triggered events and (c) earthquake-triggered events.

day when the landslides were triggered has variations among types of satellite rain; a similar variation can be seen in the axis of the antecedent rainfall. The two types of data agree on the timing of the rainfall periods but differ on the amount of millimeters of rain per day. To distinguish patterns in the rainfall information, short-term rainfall was plotted against long-term antecedent rainfall, as is shown in Figure 13. IMERG data draws a triangular pattern in the three scatter plots Fig. 13(a-c), completely forming a spaced clustering of the data over 30 mm in the short-term rainfall of 5 days and over 500 mm in the antecedent rainfall. A different pattern is shaped by CHIRPS; the data in Fig. 13(d-e) align the data from 500 mm to 1100 mm in the antecedent rainfall, followed by a less aligned clustering in Fig. 13(f), starting over 30 mm in the short-term rainfall of 5 days and similar limits of long-term rainfall as Fig. 13(c).

As Colombia is on the equator line, the patterns of rainfall are influenced by the ENSO. Figure 14 relates the occurrence of events with the chronology of the ONI. Applying the conventional $\pm 0.5\,^{\circ}\mathrm{C}$ thresholds, three of the eleven rainfall-triggered events occurred under El Niño conditions (Salgar 2015, Anori 2023, Girardota 2023), one under La Niña (Dabeiba 2020), and the remaining seven under neutral conditions (Mocoa 2017, Jerico 2019, Anori 2020, Yali 2020, Santo Domingo 2021, Cerro Bravo 2024, Altavista 2025).

4.5 Multivariate analysis

The PCA shows how the variables structure the morphometric space of the inventories, while the ICC quantifies how much of the variation of each variable can be attributed to differences between inventories. The first two panels of Fig. 15 therefore answer complementary questions: panel (a) describes how the variables relate to each other and where the inventories are positioned within

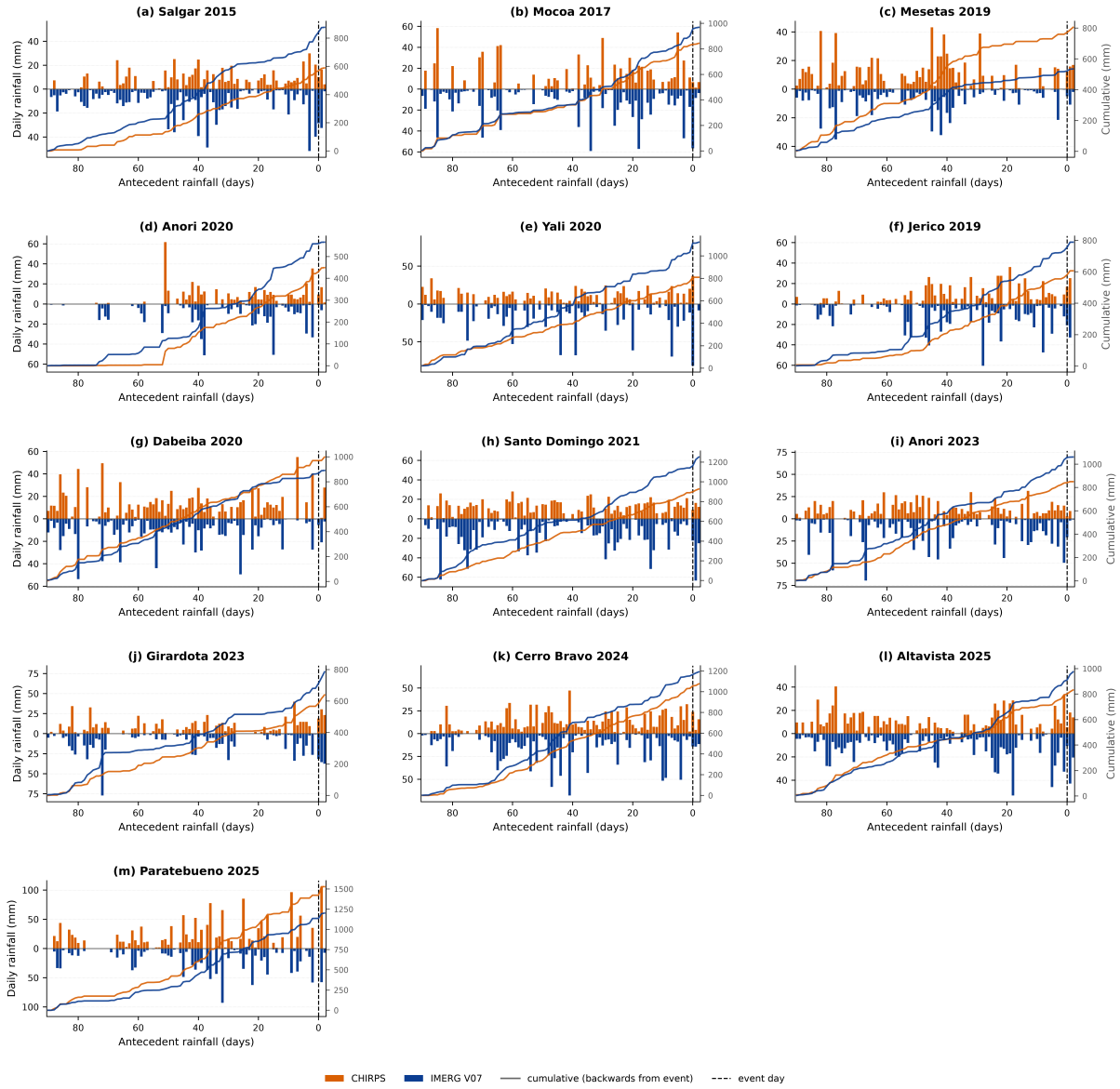


Figure 12: Daily rainfall over the 90 days preceding each event, from CHIRPS (upward, orange) and IMERG V07 (downward, blue). Solid lines show the cumulative rainfall integrated backwards from the event day (dashed vertical line, right-hand axis).

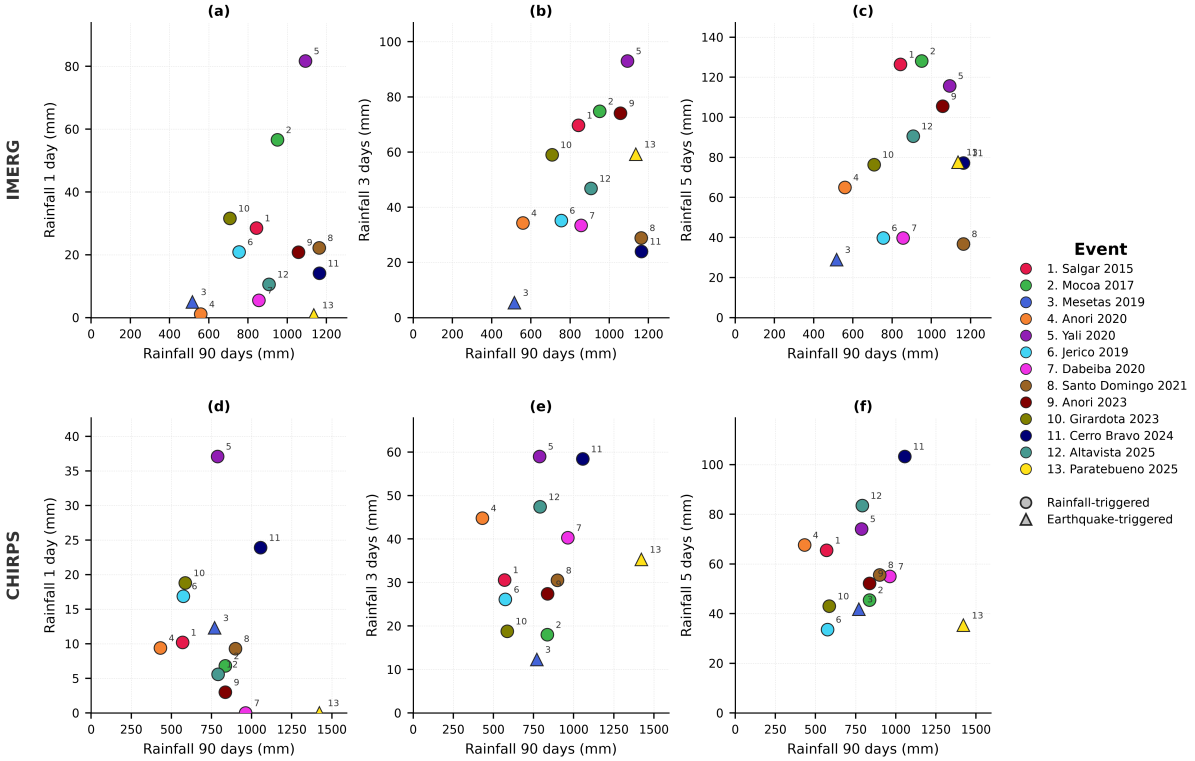


Figure 13: Short-duration rainfall (1, 3 and 5 days) plotted against 90-day antecedent rainfall for each event, from IMERG (a–c) and CHIRPS (d–f).

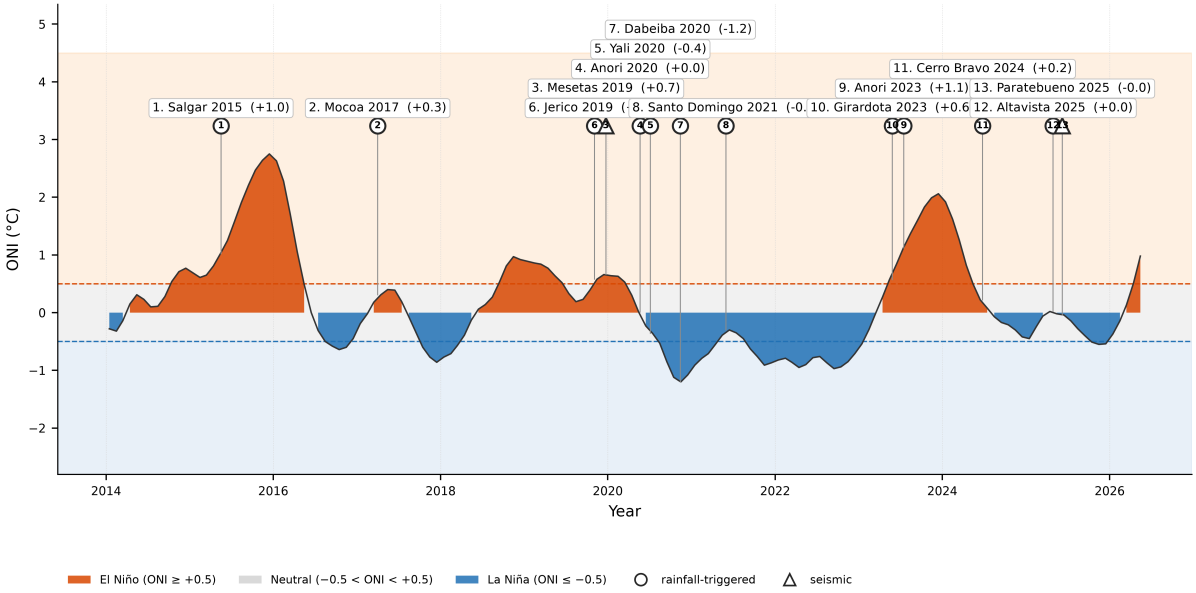


Figure 14: Chronology of the compiled events relative to the Oceanic Niño Index (ONI).

the multivariate space, and panel (b) describes the proportion of the variability of each variable that is associated with differences between inventories. The principal component analysis was carried out with nine polygon-level variables (Figure 15a). The first two components account for 25.6 % and 18.6 % of the total variance. On PC1, slope, roughness and $\log_{10}$ area point towards positive values, while local density points towards negative values. On PC2, $\log_{10}$ distance to drainage, HAND and relative elevation point towards positive values, whereas $\log_{10}$ flow accumulation points towards negative values. The inventories show different positions within this space, although most centroids remain relatively close to the origin. For example, Mesetas (2019) is positioned towards positive PC1, in the direction of slope, roughness and $\log_{10}$ area, whereas Anori (2023) is positioned towards negative PC1, closer to the direction of local density and $\log_{10}$ distance to faults.

The variance components of each variable are presented in Fig. 15b. Roughness reaches 51.8 %, so about half of its variability is associated with differences between inventories and the remaining 48.2 % with differences among the landslides of a single inventory. Local density follows with 45.6 %, slope with 38.7 %, and distance to faults with 30.8 %. The remaining five variables are between 11 % and 21 %: flow accumulation (20.8 %), relative elevation (19.7 %), HAND (19.2 %), area (18.4 %) and distance to drainage (11.1 %). For distance to drainage, 88.9 % of its variability occurs within the inventories rather than between them. Finally, Figure 15c shows the distribution of the individual landslide polygons and the centroid of each inventory in the PC1-PC2 space. Most of the thirteen inventory centroids are located close to the origin, while the polygons within each inventory extend across a relatively broad portion of the PCA space.

5 Discussion

This research compiled 13 landslide events during the recent decade (2015-2025). Most of them were rainfall-triggered due to the natural conditions of the study area, long tropical rainy seasons combined with topographical and lithological aspects of the northern Andes. In this section we discuss the key findings of the analysis. First of all, many developments in remote sensing during the last decades have provided the possibility to carry out this type of study; satellite images from Sentinel-2 give free access to download images and create new inventories to find key patterns in the analyzed data. The availability of the input data constrains the list of events

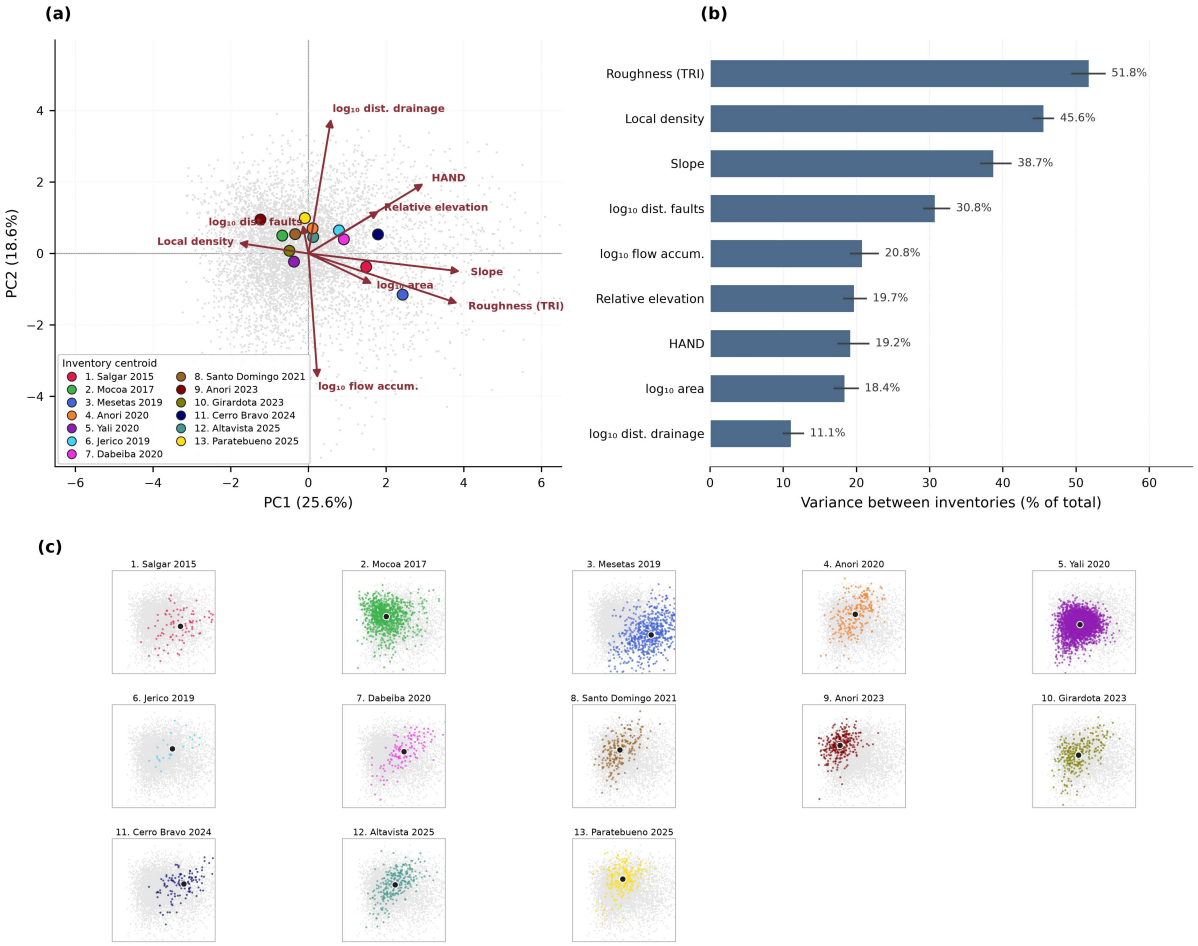


Figure 15: Morphometric variability among landslide inventories. (a) PCA distribution of the landslide inventories based on their morphometric variables. (b) Proportion of the total variance associated with differences among inventories for each morphometric variable, expressed as the intraclass correlation coefficient (ICC). (c) Each inventory highlighted over the total point cloud, with its centroid marked.

to be explored. Many of the reported landslide events that occurred before 2015 lack the main data to be included in this study, such as San Carlos, 1990; Río Fraile, 1994; La Estrella, 2000; and Tarazà, 2007 Palacio Cordoba (2023). Additionally, many landslide events have occurred in remote forested areas, where very small communities could have been affected and the local institutions never report these events. Interesting efforts have been achieved in terms of reporting the events; examples like the landslides events in Anori, 2020, and Anori, 2023, reported in this study, were documented by governmental risk management institutions and local journalism. This is an example of advancements in the importance of reporting natural hazards in a remote municipality away from the main cities in an undeveloped country. Similar efforts should continue to document and analyze this type of event in remote rural areas by institutions and academia to expand the availability and diversity of data.

The analysis of the area shows that multiple-occurrence landslide events are influential in landscape evolution. In a single event, hundreds of hectares can change land use, for example, from forest or agricultural land to bare soil, which is then prone to a higher rate of erosion and loss of productive land for human activities. An example of this is Yali (2020), where in an area of 25,000 hectares, more than 4,000 landslides of varying sizes modified a rural landscape, affecting dozens of families. The area analysis shows a pattern between the frequency of landslides and their contribution to the total affected area. Multiple-occurrence landslide events affect settlements exponentially and in different directions and magnitudes compared to a single landslide event, which might only affect roads or isolated settlements. More than 92% of the landslides between 100 and 5,000 m^2 represent about half of the affected area. The remaining 7% represents landslides on the order of 0.5 to 100 hectares. Although they may be fewer in number, these are the most significant due to their greater destructive capacity, as in Paratebueno (2025), where a 100-hectare landslide caused the greatest damage.

The exploration of morphometric variables revealed patterns and findings. Variables such as slope, distance to drainage, roughness, and flow accumulation showed consistency in distinguishing landslides from non-landslides. The average slope is steeper in landslide-affected areas, the average drainage distance is shorter than the distance to landslides, and average roughness and flow accumulation are higher in landslide zones. On the other hand, although the direction of whether a variable value is lower or higher is consistent for these four variables, the magnitude in each event is different; in some events, the difference in average slope between landslides and

non-landslides areas is much greater than in others, indicating that morphometric controls are partially dependent on the local geomorphological context.

Individual variables showed different degrees of separation, but landslide occurrence is likely controlled by the combination of several terrain characteristics. In this study, slope and distance to drainage were the variables with the greatest consistency in distinguishing between multiple landslide events. This could be due to topographic convergence, drainage concentration, channel-hillslope interaction, and local hydrological conditions. These variables could be included as predictors in susceptibility analyses in the Colombian Andes, given their consistent separation of landslide-prone and non-landslide-prone terrain across the analyzed events. Other variables, such as roughness, flow accumulation, HAND, and TWI, showed a lesser degree of distinction but could have the potential to be studied in other areas.

Regarding landslide density, few studies have analyzed this variable in multiple-occurrence landslide events in the Colombian Andes. The results of our density analysis in Mesetas, 2019, are consistent with the methodology applied by García-Delgado and Contreras (2021) in the same event, with maximum concentrations of 10 to 20 landslides per km^2. The results of the spatial density analysis revealed that the patterns of rainfall-triggered landslides were characterized by elongated clusters, with the highest concentrations toward their centers. In contrast, earthquake-triggered landslides showed scattered and loosely connected cores, resulting in lower spatial densities. Although the selected radius largely determines the density values obtained for a landslide inventory, the median landslide area density and median landslide number density indicate that the two earthquake-triggered events were less dense than the rainfall-triggered events. In recent decades, with the widespread availability of remote sensors, there are few recorded earthquake-triggered landslides in the study area; therefore, a limitation of this research is the small sample size of these events. Future events of this type could be used to compare this analysis.

Additionally, the density analysis revealed that the concentration of landslides alone does not necessarily control the percentage of affected area, because the average size of the landslides within an event also influences it. Two events can have similar numerical densities but different percentages of affected area due to differences in landslide size. Regarding landslide orientation, the analysis revealed that slope had a more consistent relationship with landslide occurrence than aspect across the different triggering mechanisms. The preference for landslides increased toward the highest slope classes, particularly above 40°, in all three inventories. The earthquake-

triggered landslides showed a stronger directional pattern, with high preference values distributed across most sectors and a marked reduction in the NW quadrant. This difference from the rainfall-triggered events suggests that the relationship between aspect and landslide occurrence may depend on the triggering mechanism.

The results of the lithological exploration and soil type were consistent with previous studies; intrusive rocks were the most frequent rock type across the multiple-occurrence landslide events, appearing in 7 of the 13 events. As documented in Aristízabal and Sánchez (2020), granitic rocks are the most frequent material where concatenated events such as torrential flows occurred. The second most frequent rock type was foliated metamorphic rocks, which were dominant in three events. Part of this lithological dominance is due to the fact that most of the events were documented in the central mountain range of the Colombian Andes, which is composed mainly of these two lithologies. The events that contributed the majority of sedimentary rocks correspond to the two earthquake-triggered events, both of which are located in the eastern mountain range bordering the Llanos foothills. Regarding soil grain size, more than 70% of the mapped landslides occurred on soils inferred to be coarse-grained, which is consistent with the occurrence of previous events in granular residual soils and saprolites reported for landslide-prone hillslopes in the Colombian Andes Palacio Cordoba et al. (2020).

Rainfall analysis was conducted using CHIRPS and IMERG satellite products due to the lack of gauge rainfall data for all study areas. This lack of data has an implication: as shown in previous studies, satellite rainfall data tend to underestimate rainfall compared to gauge measurements Urrea et al. (2016). Furthermore, discrepancies were found in short- and long-term rainfall magnitudes for all events, consistent with results from other studies Valencia et al. (2023). This is largely due to the inherent nature of how each instrument acquires data, as well as differences in spatial and temporal resolution. However, both sensors detected the timing of periods when rainfall occurred and did not. This is reflected in the similarity of the clustering patterns in Figures 13(c) and 13(f), where data cluster above 30 mm for short-term rainfall and above 500 mm for long-term antecedent rainfall. Although, as observed throughout the figure, the position of each event differs in the CHIRPS and IMERG data, the correlation only appears at the limits in rainfall values. Regarding the occurrence of multiple-occurrence landslides in relation to ENSO, no direct influence is reported for the occurrence of most of the collected events; therefore, in the Colombian Andes, anomalous ENSO conditions are not required to trigger a multiple-occurrence landslide event. Seven out of eleven occurred under neutral conditions.

However, in the northern part of the study area, the increased frequency of individual landslides is associated with the cold phase (La Niña) of ENSO Naranjo Bedoya et al. (2019); Vega et al. (2024).

The PCA and ICC analyses provide complementary evidence that multiple-occurrence landslide inventories in the Colombian Andes share a common morphometric setting while still exhibiting measurable differences between events. The PCA showed that the inventory centroids are concentrated around the center of the multivariate space, whereas the individual landslides of each inventory occupy a much broader range of conditions. The orientation of the PCA highlights the main geomorphological gradients controlling the events. The first component is primarily associated with terrain slope, roughness, and landslide area, in contrast to local landslide density. This component describes the setting in which each event occurred: how steep and how dissected the terrain is. The second component is mainly related to topographic position, represented by HAND, relative elevation, and distance to drainage. It is important to highlight that the first two principal components explain 44.2% of the total variance, meaning that more than half of the variability is contained in subsequent components and is therefore not represented in the two-dimensional visualization. Finally, the ICC results further clarify which variables are characteristic of individual events and which are more consistent across inventories. Roughness showed the highest between-inventory variance (51.8%), followed by local density and slope. This indicates that these variables are the most effective for distinguishing one multiple-occurrence event from another, reflecting differences in terrain morphology and in the spatial organization of landslides. On the other hand, variables such as distance to drainage, HAND, relative elevation, and flow accumulation exhibited larger within-inventory variability. This could indicate that hydrological and topographic-position variables operate mainly at the local hillslope scale rather than defining the overall characteristics of a landslide event.

6 Conclusions

This research involved a search for multiple-occurrence landslide events, collecting 8,088 samples, along with a spatial analysis that revealed key findings in occurrence patterns. Nine of the inventories were mapped in this work through manual mapping over pre- and post-event Sentinel-2 composites, and the remaining ones were extracted from previous studies. In terms of morphometry, slope, distance to drainage, roughness, and flow accumulation played a role in

highlighting the difference between landslides and non-landslide terrain throughout all events. The first two were the most consistent in the magnitude of the difference in each event and are the variables we would prioritize as predictors for susceptibility analysis. Other variables describing the landslides provided patterns in distinguishing between events triggered by rain and earthquakes. The concentration and organization of rainfall events formed elongated clusters, while those triggered by earthquakes exhibited scattered and loosely connected cores; the latter also showed the lowest densities.

The results regarding lithology and soil type confirm previous studies showing that hazards such as debris floods and debris flows were more frequent in soils of intrusive rocks in the Colombian Andes. Most of the landslides triggered by the events were in soils associated with coarse-grained particles, which could also be considered in susceptibility analyses. Regarding rainfall patterns, clear clusters were observed for short-term 5-day rainfall (over 30 mm) and 90-day antecedent rainfall (over 500 mm) for both types of satellite rainfall data (CHIRPS and IMERG). Seven of the eleven rainfall-triggered events occurred under neutral ENSO conditions and three during the warm phase (El Niño). Therefore, anomalous ENSO states do not correlate directly with multiple-occurrence landslides in the Colombian Andes. On the other hand, PCA and ICC analysis indicate that the inventories share a broad morphometric space; however, differences are marked by some variables. Slope, roughness, and local density differentiate the events, while distance to drainage, HAND, relative elevation, and flow accumulation show greater internal variability within each inventory.

In the decade from 2015 to 2025, at least 13 multiple-occurrence landslide events were reported in the Colombian Andes. This frequency implies an average of more than one event per year and represents a level of activity not previously documented in the region. Advances in remote sensing over the last few decades have allowed, for the first time, the compilation of an inventory of multiple-occurrence landslide events for the study area, opening avenues for future research questions about the phenomenon. However, the compilation is limited to events for which suitable satellite imagery exists, excluding earlier events and likely underrepresenting remote areas where small communities were affected and no institutional report was produced. Continued documentation of these events by both institutions and academia would expand the diversity of the dataset and allow the comparisons presented here to be tested with a larger sample, as well as facilitate further analysis for risk management and reduction. The cumulative damage from these events has resulted in approximately 450 deaths, along with countless losses

to infrastructure, social dynamics, and ecosystems. Risk management institutions should pay special attention to these events, as the density and magnitude of the landslides can cause significant losses.

Code and data availability

Data availability on request

Author contributions

E.C.; methodology, E.C. and E.V.; software, E.C. ; validation, E.M., A.O., D.R. and A.M.; formal analysis, E.C. and E.M.; investigation, E.C., E.M., A.O., D.R. and A.M.; resources, M.G., A.O. and A.M.; data curation, E.C., A.O. and A.M.; writing—original draft preparation, E.C.; writing—review and editing, E.C. and A.M.; visualization, E.C.; supervision, E.M., M.G., D.R. and A.M.; project administration, M.G., D.R. and A.M.; funding acquisition, M.G. All authors have read and agreed to the published version of the manuscript.

Competing interests

The authors declare no conflicts of interest.

Acknowledgements

Authors would like to thank the local departmental government, Gobernación de Antioquia, through the SAMA program (Alert and Monitoring System of Antioquia) funded by the Administrative Department for Risk and Disaster Management (DAGRAN), managed by Universidad EAFIT, with contract No. 25CT424C2101.

References

Arango-Carmona, M. I., Voit, P., Hürlimann, M., Aristizábal, E., and Korup, O. (2025). Hillslope torrential hazard cascades in tropical mountains. *Natural Hazards and Earth System Sciences*, 25(10):3641–3663.

Aristizábal, E., García-Aristizábal, E. F., Guzmán-Martínez, J. C., García-Ramírez, A., Gómez-Ríos, S., Castillo-Cardona, E., and Zapata-Valencia, D. (2025). Amenazas naturales concatenadas: avenida torrencial del 13 de noviembre de 2020 en el municipio de Dabeiba (Colombia). *Boletín de Geología*, 47(2):107–123.

Aristízabal, E. and Korup, O. (2025). Linking landslide patterns to transient landscapes in the northern Colombian Andes. *Journal of Geophysical Research: Earth Surface*, 130(3):e2024JF008027.

Aristízabal, E. and Sánchez, O. (2020). Spatial and temporal patterns and the socioeconomic impacts of landslides in the tropical and mountainous Colombian Andes. *Disasters*, 44(3):596–618.

Aristizábal-Giraldo, E. V. and Ruiz-Vásquez, D. (2023). Landslide susceptibility assessment in scarce-data regions using remote sensing data. *Revista Facultad de Ingeniería Universidad de Antioquia*.

Bedoya-Soto, J. M., Aristizábal, E., Carmona, A. M., and Poveda, G. (2019). Seasonal shift of the diurnal cycle of rainfall over medellin's valley, central andes of colombia (1998–2005). *Frontiers in Earth Science*, 7:92.

Costa, J. E. and Schuster, R. L. (1988). The formation and failure of natural dams. *Geological Society of America Bulletin*, 100(7):1054–1068.

Crozier, M. J. (2017). A proposed cell model for multiple-occurrence regional landslide events: Implications for landslide susceptibility mapping. *Geomorphology*, 295:480–488.

Dadson, S. J., Hovius, N., Chen, H., Dade, W. B., Lin, J.-C., Hsu, M.-L., Lin, C.-W., Horng, M.-J., Chen, T.-C., Milliman, J., and Stark, C. P. (2004). Earthquake-triggered increase in sediment delivery from an active mountain belt. *Geology*, 32(8):733–736.

Dahal, R. K. and Hasegawa, S. (2008). Representative rainfall thresholds for landslides in the Nepal Himalaya. *Geomorphology*, 100(3–4):429–443.

Dai, F. C., Xu, C., Yao, X., Xu, L., Tu, X. B., and Gong, Q. M. (2011). Spatial distribution of landslides triggered by the 2008 Ms 8.0 Wenchuan earthquake, China. *Journal of Asian Earth Sciences*, 40(4):883–895.

Fan, X., Scaringi, G., Korup, O., West, A. J., van Westen, C. J., Tanyas, H., Hovius, N., Hales, T. C., Jibson, R. W., Allstadt, K. E., Zhang, L., Evans, S. G., Xu, C., Li, G., Pei, X., Xu, Q.,

and Huang, R. (2019). Earthquake-induced chains of geologic hazards: Patterns, mechanisms, and impacts. *Reviews of Geophysics*, 57(2):421–503.

Froude, M. J. and Petley, D. N. (2018). Global fatal landslide occurrence from 2004 to 2016. *Natural Hazards and Earth System Sciences*, 18(8):2161–2181.

García-Delgado, H. and Contreras, N. (2021). Historical distribution for landslides triggered by earthquakes in the Colombian region. In Cabrera, M. A. and Prada-Sarmiento, L. F., editors, *Proceedings of the 13th International Symposium on Landslides*, pages 1–8, Cartagena, Colombia. ISSMGE.

García-Delgado, H., Machuca, S., and Medina, E. (2019). Dynamic and geomorphic characterizations of the Mocoa debris flow (March 31, 2017, Putumayo Department, southern Colombia). *Landslides*, 16(3):597–609.

García-Delgado, H., Petley, D. N., Bermúdez, M. A., and Sepúlveda, S. A. (2022). Fatal landslides in Colombia (from historical times to 2020) and their socio-economic impacts. *Landslides*, 19(7):1689–1716.

Ghorbanzadeh, O., Xu, Y., Ghamisi, P., Kopp, M., and Kreil, D. (2022). Landslide4sense: reference benchmark data and deep learning models for landslide detection. *IEEE Transactions on Geoscience and Remote Sensing*, 60:1–17.

Giordan, D., Manconi, A., Facello, A., Baldo, M., Dell'Anese, F., Allasia, P., and Dutto, F. (2015). Brief Communication: The use of an unmanned aerial vehicle in a rockfall emergency scenario. *Natural Hazards and Earth System Sciences*, 15(1):163–169.

Gómez Cardona, F., Aristízabal Giraldo, E., and Mergili, M. (2025). Modelling debris flood propagation in scarce data terrain, case study in the Colombian Andes. *Journal of South American Earth Sciences*, 165:105660.

Guzzetti, F., Mondini, A. C., Cardinali, M., Fiorucci, F., Santangelo, M., and Chang, K.-T. (2012). Landslide inventory maps: New tools for an old problem. *Earth-Science Reviews*, 112(1–2):42–66.

Hermelin, M., Mejía, O., and Velásquez, E. (1992). Erosional and depositional features produced by a convulsive event, San Carlos, Colombia, September 21, 1990. *Bulletin of the International Association of Engineering Geology*, 45(1):89–95.

Hidalgo, C. A. and Vega, J. A. (2021). Probabilistic landslide risk assessment in water supply basins: La Liboriana River Basin (Salgar-Colombia). *Natural Hazards*, 109(1):273–301.

Hovius, N., Meunier, P., Lin, C.-W., Chen, H., Chen, Y.-G., Dadson, S., Horng, M.-J., and Lines, M. (2011). Prolonged seismically induced erosion and the mass balance of a large earthquake. *Earth and Planetary Science Letters*, 304(3–4):347–355.

Huang, R. and Fan, X. (2013). The landslide story. *Nature Geoscience*, 6(5):325–326.

Kirschbaum, D. B., Adler, R., Hong, Y., Hill, S., and Lerner-Lam, A. (2010). A global landslide catalog for hazard applications: method, results, and limitations. *Natural Hazards*, 52(3):561–575.

Li, G., West, A. J., Densmore, A. L., Jin, Z., Parker, R. N., and Hilton, R. G. (2014). Seismic mountain building: Landslides associated with the 2008 Wenchuan earthquake in the context of a generalized model for earthquake volume balance. *Geochemistry, Geophysics, Geosystems*, 15(4):833–844.

Lin, C.-W., Chang, W.-S., Liu, S.-H., Tsai, T.-T., Lee, S.-P., Tsang, Y.-C., Shieh, C.-L., and Tseng, C.-M. (2011). Landslides triggered by the 7 August 2009 Typhoon Morakot in southern Taiwan. *Engineering Geology*, 123(1–2):3–12.

Malamud, B. D., Turcotte, D. L., Guzzetti, F., and Reichenbach, P. (2004). Landslide inventories and their statistical properties. *Earth Surface Processes and Landforms*, 29(6):687–711.

Marc, O., Hovius, N., Meunier, P., Uchida, T., and Hayashi, S. (2015). Transient changes of landslide rates after earthquakes. *Geology*, 43(10):883–886.

Marín, R. J., Velásquez, M. F., and Sánchez, O. (2021). Applicability and performance of deterministic and probabilistic physically based landslide modeling in a data-scarce environment of the Colombian Andes. *Journal of South American Earth Sciences*, 108:103175.

Meena, S. R., Nava, L., Bhuyan, K., Puliero, S., Soares, L. P., Dias, H. C., Floris, M., and Catani, F. (2023). HR-GLDD: a globally distributed dataset using generalized deep learning (DL) for rapid landslide mapping on HR satellite imagery. *Earth System Science Data*, 15(8):3283–3298.

Mesa, Ó., Poveda, G., Vélez-Upegui, J. I., Mejía Valencia, J. F., Hoyos Ortiz, C. D., Mantilla Gutiérrez, R., Barco Mejía, O. J., Cuartas Pineda, L. A., Botero Hernández, B., and Montoya, M. (2000). Distribución espacial y ciclos anual y semianual de la precipitación en colombia. In *XIV Seminario de Hidráulica e Hidrología*, number 1, pages 1–9.

Meunier, P., Hovius, N., and Haines, J. A. (2008). Topographic site effects and the location of earthquake induced landslides. *Earth and Planetary Science Letters*, 275(3–4):221–232.

Naranjo Bedoya, K., Aristizábal Giraldo, E. V., and Morales Rodelo, J. A. (2019). Influencia del ENSO en la variabilidad espacial y temporal de la ocurrencia de movimientos en masa desencadenados por lluvias en la región Andina colombiana. *Ingeniería y Ciencia*, 15(29):11–42.

Nieto, S., Aristízabal, E., and Ozturk, U. (2025). Coupled evolution of a city and landslides. *Environmental Research Letters*, 20(5):054001.

Noriega-Londoño, S., Restrepo-Moreno, S. A., Vinasco, C., Bermúdez, M. A., and Min, K. (2020). Thermochronologic and geomorphometric constraints on the Cenozoic landscape evolution of the northern Andes: Northwestern central cordillera, Colombia. *Geomorphology*, 351:106890.

Notti, D., Cignetti, M., Godone, D., and Giordan, D. (2023). Semi-automatic mapping of shallow landslides using free Sentinel-2 images and Google Earth Engine. *Natural Hazards and Earth System Sciences*, 23(7):2625–2648.

Ozturk, U., Bozzolan, E., Holcombe, E. A., Shukla, R., Pianosi, F., and Wagener, T. (2022). How climate change and unplanned urban sprawl bring more landslides. *Nature*, 608(7922):262–265.

Palacio Cordoba, J., Mergili, M., and Aristízabal, E. (2020). Probabilistic landslide susceptibility analysis in tropical mountainous terrain using the physically based r.slope.stability model. *Natural Hazards and Earth System Sciences*, 20(3):815–829.

Palacio Cordoba, J. A. (2023). Shallow landslide cluster propagation in tropical mountainous terrains. case study Colombian Andes. M.Sc. thesis, Universidad Nacional de Colombia, Facultad de Minas, Medellín, Colombia.

Pérez-Consuegra, N., Ott, R. F., Hoke, G. D., Galve, J. P., Pérez-Peña, V., and Mora, A. (2021). Neogene variations in slab geometry drive topographic change and drainage reorganization in the northern Andes of Colombia. *Global and Planetary Change*, 206:103641.

Poveda, G. (2004). La hidroclimatología de colombia: una síntesis desde la escala inter-decadal hasta la escala diurna. *Revista de la Academia Colombiana de Ciencias Exactas, Físicas y Naturales*, 28(107):201–222.

Poveda, G., Waylen, P. R., and Pulwarty, R. S. (2006). Annual and inter-annual variability of the present climate in northern South America and southern Mesoamerica. *Palaeogeography, Palaeoclimatology, Palaeoecology*, 234(1):3–27.

Prada-Sarmiento, L. F., Cabrera, M. A., Camacho, R., Estrada, N., and Ramos-Cañón, A. M. (2019a). The Mocoa event on March 31 (2017): analysis of a series of mass movements in a tropical environment of the Andean-Amazonian piedmont. *Landslides*, 16(12):2459–2468.

Prada-Sarmiento, L. F., Cabrera, M. A., Camacho, R., Estrada, N., and Ramos-Cañón, A. M. (2019b). The Mocoa Event on March 31 (2017): analysis of a series of mass movements in a tropical environment of the Andean-Amazonian Piedmont. *Landslides*, 16(12):2459–2468.

Restrepo, C., Walker, L. R., Shiels, A. B., Bussmann, R., Claessens, L., Fisch, S., Lozano, P., Negi, G., Paolini, L., Poveda, G., Ramón, C., Scatena, M., and Velázquez, E. (2009). Landsliding and its multiscale influence on mountainscapes. *BioScience*, 59(8):685–698.

Restrepo-Moreno, S. A., Foster, D. A., Bernet, M., Min, K., and Noriega, S. (2019). Morphotectonic and orogenic development of the northern Andes of Colombia: A low-temperature thermochronology perspective. In *Geology and Tectonics of Northwestern South America: The Pacific-Caribbean-Andean Junction*, pages 749–832. Springer.

Rodríguez, E. A., Sandoval, J. H., Chaparro, J. L., Trejos, G. A., Medina, E., Ramírez, K. C., Castro, E., Castro, J. A., and Ruiz, G. L. (2017). *Guía metodológica para la zonificación de amenaza por movimientos en masa escala 1:25.000*. Servicio Geológico Colombiano, Bogotá.

Saito, H., Nakayama, D., and Matsuyama, H. (2010). Relationship between the initiation of a shallow landslide and rainfall intensity–duration thresholds in Japan. *Geomorphology*, 118(1–2):167–175.

Sánchez-Rodríguez, R. and Correa, J. (2022). Planning gaps: unexpected urban expansion in five Colombian metropolitan areas. *Buildings and Cities*, 3(1):643–661.

Segoni, S., Piciullo, L., and Gariano, S. L. (2018). A review of the recent literature on rainfall thresholds for landslide occurrence. *Landslides*, 15(8):1483–1501.

Sepúlveda, S. A. and Petley, D. N. (2015). Regional trends and controlling factors of fatal landslides in Latin America and the Caribbean. *Natural Hazards and Earth System Sciences*, 15(8):1821–1833.

Servicio Geológico Colombiano (2021). *Guía metodológica para zonificación de amenaza por avenidas torrenciales*. Servicio Geológico Colombiano, Bogotá.

Tanyaş, H., Allstadt, K. E., and van Westen, C. J. (2018). An updated method for estimating landslide-event magnitude. *Earth Surface Processes and Landforms*, 43(9):1836–1847.

Tanyaş, H., van Westen, C. J., Allstadt, K. E., Nowicki Jessee, M. A., Görüm, T., Jibson, R. W., Godt, J. W., Sato, H. P., Schmitt, R. G., Marc, O., and Hovius, N. (2017). Presentation and analysis of a worldwide database of earthquake-induced landslide inventories. *Journal of Geophysical Research: Earth Surface*, 122(10):1991–2015.

Tehrani, F. S., Calvello, M., Liu, Z., Zhang, L., and Lacasse, S. (2022). Machine learning and landslide studies: recent advances and applications. *Natural Hazards*, 114(2):1197–1245.

Urrea, V., Ochoa, A., and Mesa, O. (2016). Validación de la base de datos de precipitación CHIRPS para Colombia a escala diaria, mensual y anual en el período 1981–2014. In *XXVII Congreso Latinoamericano de Hidráulica*, Lima, Peru. 26–30 September 2016.

Valencia, S., Marín, D. E., Gómez, D., Hoyos, N., Salazar, J. F., and Villegas, J. C. (2023). Spatio-temporal assessment of gridded precipitation products across topographic and climatic gradients in Colombia. *Atmospheric Research*, 285:106643.

Vega, J., Barco, J., and Hidalgo, C. (2024). Space-time analysis of the relationship between landslides occurrence, rainfall variability and ENSO in the Tropical Andean Mountain region in Colombia. *Landslides*, 21(6):1293–1314.

Velásquez, N., Hoyos, C. D., Vélez, J. I., and Zapata, E. (2020). Reconstructing the 2015 Salgar flash flood using radar retrievals and a conceptual modeling framework in an ungauged basin. *Hydrology and Earth System Sciences*, 24(3):1367–1392.

Vershel, A. and Kirschbaum, D. (2025). Open inventories of rainfall-triggered landslides. *Geoscience Data Journal*, 12(4):e70023.

Xu, C., Xu, X., Yao, X., and Dai, F. (2014). Three (nearly) complete inventories of landslides triggered by the May 12, 2008 Wenchuan Mw 7.9 earthquake of China and their spatial distribution statistical analysis. *Landslides*, 11(3):441–461.

Zhang, S. and Zhang, L. M. (2017). Impact of the 2008 Wenchuan earthquake in China on subsequent long-term debris flow activities in the epicentral area. *Geomorphology*, 276:86–103.